



Star cluster formation in a turbulent molecular cloud self-regulated by photoionization feedback

Elena Gavagnin, Andreas Bleuler, Joakim Rosdahl, Romain Teyssier

► To cite this version:

Elena Gavagnin, Andreas Bleuler, Joakim Rosdahl, Romain Teyssier. Star cluster formation in a turbulent molecular cloud self-regulated by photoionization feedback. Monthly Notices of the Royal Astronomical Society, 2017, 472, pp.4155-4172. 10.1093/mnras/stx2222 . insu-03710598

HAL Id: insu-03710598

<https://insu.hal.science/insu-03710598>

Submitted on 1 Jul 2022

HAL is a multi-disciplinary open access archive for the deposit and dissemination of scientific research documents, whether they are published or not. The documents may come from teaching and research institutions in France or abroad, or from public or private research centers.

L'archive ouverte pluridisciplinaire **HAL**, est destinée au dépôt et à la diffusion de documents scientifiques de niveau recherche, publiés ou non, émanant des établissements d'enseignement et de recherche français ou étrangers, des laboratoires publics ou privés.

Star cluster formation in a turbulent molecular cloud self-regulated by photoionization feedback

Elena Gavagnin,¹★ Andreas Bleuler,¹ Joakim Rosdahl² and Romain Teyssier¹

¹*Institute for Computational Science, Centre for Theoretical Astrophysics and Cosmology, Universität Zürich, CH-8057 Zürich, Switzerland*

²*Univ. Lyon, Univ. Lyon1, Ens de Lyon, CNRS, Centre de Recherche Astrophysique de Lyon UMR5574, F-69230 Saint-Genis-Laval, France*

Accepted 2017 August 25. Received 2017 August 22; in original form 2017 January 26

ABSTRACT

Most stars in the Galaxy are believed to be formed within star clusters from collapsing molecular clouds. However, the complete process of star formation, from the parent cloud to a gas-free star cluster, is still poorly understood. We perform radiation-hydrodynamical simulations of the collapse of a turbulent molecular cloud using the `RAMSES-RT` code. Stars are modelled using sink particles, from which we self-consistently follow the propagation of the ionizing radiation. We study how different feedback models affect the gas expulsion from the cloud and how they shape the final properties of the emerging star cluster. We find that the star formation efficiency is lower for stronger feedback models. Feedback also changes the high-mass end of the stellar mass function. Stronger feedback also allows the establishment of a lower density star cluster, which can maintain a virial or sub-virial state. In the absence of feedback, the star formation efficiency is very high, as well as the final stellar density. As a result, high-energy close encounters make the cluster evaporate quickly. Other indicators, such as mass segregation, statistics of multiple systems and escaping stars confirm this picture. Observations of young star clusters are in best agreement with our strong feedback simulation.

Key words: stars: formation – stars: kinematics and dynamics – H II regions – galaxies: star clusters: general – galaxies: star clusters: individual: (NGC 3603 YC, Arches) – ultraviolet: stars.

1 INTRODUCTION

Establishing a full and consistent theory of star cluster formation remains an open task for the scientific community. The most widely adopted view is that star clusters form from the collapse of giant molecular clouds. On a time-scale of a few millions years, a cloud undergoes gravitational collapse and converts part of its gas into many dense molecular cores, each core leading to the formation of one or a few proto-stellar objects (see Klessen 2011; Krumholz 2014, for a review). These protostars can continue accreting material from their surroundings, and eventually become proper stellar, main sequence objects, whose stellar luminosity is high enough to inject considerable amounts of energy into their parent cloud. This stellar feedback (FB) modifies the properties of the cloud and the star formation process itself and as a result regulates the properties of the emerging star cluster, such as its dynamical state, the mass distribution and the fate of its stellar population.

Understanding the impact of stellar FB on the star cluster properties, and the transition from the initial turbulent GMC to the final gas-free association of stars (such as observed open clusters,

embedded clusters or even globular clusters) is at the moment one of the most intriguing fields of research in astrophysics, mainly because of the numerous and complex physical processes at play during the entire history of the star cluster formation.

A classic reference is the work of Lada & Lada (2003), which states that 90 per cent of stars are likely to form in star clusters. In Lada & Lada (2003), star clusters are defined as groups of at least 35 stars and with a stellar mass density of at least $1 \text{ M}_{\odot} \text{ pc}^{-3}$. These numbers can be derived by requiring that the evaporation time-scale of the star cluster is longer than 100 Myr. A more recent study by Bressert et al. (2010) revealed how the fraction of stars in the solar neighbourhood forming in clusters is strongly dependent on the adopted definition for star clusters, with values ranging between 45 and 90 per cent. They concluded that stars form within a broad and smooth distribution of surface densities, which is consistent with star formation proceeding hierarchically, within the turbulent, hierarchical structure of the parent molecular cloud, where denser regions are systematically embedded in less dense regions (Elmegreen 2006; Bastian et al. 2007).

Defining what is a truly bound cluster or an unbound stellar association is indeed not straightforward, especially when the system is young. It is only after these stellar structures have dynamically evolved that they are easier to distinguish from their

★ E-mail: gavagnin@physik.uzh.ch

environment. The identification of the fraction of stars residing within these older stellar systems is more reliable, and is observed to be around 10–30 per cent (Miller & Scalo 1978; Adamo, Östlin & Zackrisson 2011). Kruijssen (2012) shows that the cluster-formation efficiency varies from 1–70 per cent depending on the galactic gas surface densities at which the cluster forms.

It is also very important to establish what is the fraction of stars which formed in star clusters but do not reside there anymore today. This is usually referred to as a star clusters *infant mortality*, outlining the fact that when we compare the fraction of stars in young, embedded star clusters with the fraction of stars in older, open clusters, most of the clusters seems to have been disrupted during this transition from embedded to exposed (Lada & Lada 2003). Note that this interpretation assumes that the fraction of stars in star clusters is the rather old one presented in Lada & Lada (2003).

The commonly adopted picture for the cause of this infant mortality is the fast expulsion of the initial gas, leading to the rapid expansion and disruption of the star cluster. Only clusters with a star formation efficiency (SFE, i.e. the fraction of gas converted into stars) higher than 30 per cent are believed to survive the gas removal and stay bound (Hills 1980; Lada, Margulis & Dearborn 1984; Bastian & Goodwin 2006). Yet, the SFE is not the only parameter that can decide whether a star cluster will survive gas expulsion. Two other important factors are the time-scale of gas removal and the actual dynamical state of the star cluster right before expulsion. Regarding the first point, it has been shown for example that systems with SFE as low as 10 per cent can remain bound, as long as the gas is removed slowly and adiabatically (Baumgardt & Kroupa 2007). The second factor has been pointed out by Goodwin (2009), showing a strong dependence of the star cluster mass-loss (hence survival) on the virial ratio of the emerging star cluster. Indeed, if the system is sub-virial before gas is expelled, it can survive even with SFE lower than 30 per cent. Conversely, an initially supervirial system, even with an SFE as high as 50 per cent, will be at edge of survivability (Goodwin 2009).

Kruijssen (2012) questions the importance of gas expulsion in determining the fate of the star cluster and justifies the observed poor number of bound clusters as direct result of the star formation process. According to the author, most of the natal cloud is characterized by low SFE and will therefore form dispersed structure, while only the few sites of high SFE will give birth to bound star clusters.

The SFE within star-forming molecular clouds is poorly understood from theoretical grounds. Simple models based only on self-gravitating turbulence predict a very high SFE, higher than 90 per cent, meaning that star formation occurs during one free-fall time of the parent cloud, in contradiction with observational constraints (Padoan et al. 2014).

Stellar FB has been invoked to reduce the SFE by terminating star formation in giant molecular clouds (see the review by Dale 2015, and references therein). Stellar FB is a broad term that refers to the injection of mass, momentum and energy by stars and protostars into the star-forming gas itself. The different mechanisms of stellar FB are photoionization from massive main sequence stars, infrared and optical radiation from accreting protostars, radiation pressure associated to these various types of radiation, proto-stellar jets, stellar winds from main sequence or post-main sequence stars, supernovae (SNe) explosions. Although all these ingredients are likely to play an important role in regulating the SFE and in setting the properties of the emerging star clusters, they act on different spatial and temporal scales, and are associated with stars of different masses. During the first Myrs of a star cluster life, before the first OB stars

form, FB modes from pre-main sequence stars play a significant role. These include jets, deuterium-burning and accretion FB. Pre-main sequence FB is generally not effective on large-scale and does not drive the process of gas clearing; however, it has been shown to be able to sustain turbulence and reduce the conversion rate of gas into stars (Krumholz, Klein & McKee 2012; Federrath 2015). Moreover radiation focusing in the direction of outflow cavities prevents the formation of radiation pressure-supported gas bubbles, diminishing the radiative heating and outward radiation force exerted on the infalling cloud gas (Cunningham et al. 2011), resulting in higher mass accretion on to the protostar. Disc fragmentation is also suppressed as a result of thermal FB from protostars (Offner et al. 2009), affecting the multiplicity of stellar systems.

On the observational side, several surveys can be used to cast light on the star cluster formation process. The MYSTiX survey (Feigelson et al. 2013), for example, is targeting massive star forming regions and has revealed that star clusters are frequently divided into sub-clusters (Kuhn et al. 2015). We now have evidence that these sub-clusters are expanding or merging, with clear signs of ongoing dynamical relaxation. For example, we observe mass segregation (see Section 3.3 for a definition) down to $1.5 M_{\odot}$ (Kuhn et al. 2015). Similarly, Da Rio, Tan & Jaehnig (2014) have studied the morphology and the dynamical state of the Orion nebula cluster. They concluded that the core appears rounder and smoother than the outskirts, which is consistent with ongoing dynamical processing.

The Gaia-ESO Survey (Gilmore et al. 2012) has recently discovered several kinematically distinct populations in the young star cluster Gamma Velorum, surrounding the γ^2 Velorum binary in the Vela OB2 association. According to Jeffries et al. (2014), the first component of Gamma Velorum is a bound remnant of an initially larger cluster, formed in a dense region of the Vela OB2 association, that has been partially disrupted by gas expulsion. The second component consists of a scattered population of unbound stars born later (as indicated by lithium depletion) in less dense regions. The gas surrounding this second population was probably evaporated by the radiation coming from the first one, quenching the star formation episode quite abruptly.

In general, very young star clusters, sometimes still embedded in their parent gas cloud, are ideal laboratories to study the effect and phenomenology of stellar FB and gas expulsion. In the Milky Way, the so-called ‘starburst star clusters’ (e.g. NGC 3603 YC, Quintuplet, Arches, Westerlund 1 and 2) represent the youngest (<5 Myr) and more actively star-forming clusters (Brandner 2008). NGC 3603 YC, for example, is only ~ 1 Myr old, and is surrounded by glowing interstellar gas and obscuring dust (Röllig et al. 2011). The Arches, the second youngest with an age of ~ 2.5 Myr, is already free of any gas in its centre (Stolte et al. 2003) with a clear X-ray signature of hot outflowing gas (Yusef-Zadeh et al. 2002). These newborn star clusters are characterized by the presence of strongly ultra-violet (UV) radiation from O and B stars that ionizes the nebula and disperses the gas (Crowther et al. 2010; McLeod et al. 2016).

On the theoretical side, the challenge of modelling star clusters is due to the lack of a complete theory of star formation. This is an inherently multiscale, multiphysics problem, with a central role played by FB mechanisms. We point to the reviews by Dale (2015) and Krumholz et al. (2014) for a detailed presentation of the problem. Here we present only a few selected earlier studies, relevant for our work that focuses specifically on the star cluster formation process.

Walch et al. (2012); Walch et al. (2013) modelled fractal clouds by means of 3D smoothed particle hydrodynamics (SPH) simulations and explored the effect of an ionizing O-star at the centre of a

$10^4 M_{\odot}$ cloud. They found that some global properties, such as the total outflow rate, the distribution of gas into high- and low-density and the injected kinetic energy are all independent of the fractal dimension, while the statistical properties of the triggered star formation events and the shell morphology both appear to correlate with the cloud fractal dimension.

Fujii & Portegies Zwart (2015), Fujii (2015) and Fujii & Portegies Zwart (2016) used direct N -body simulations, starting from initial conditions drawn from the results of previous SPH simulations of turbulent molecular clouds. Because the adopted SPH resolution was relatively low (~ 0.1 pc), the authors could not resolve the formation of individual stars, but could still capture the clumpy structure of the gas. After one free-fall time of the initial gas cloud, they stopped the hydrosimulation and replaced dense enough gas particles with stellar particles, assuming an SFE (or gas to star conversion factor) depending on the local gas density. The remaining gas particles were removed instantaneously and the stellar particles dynamics was integrated further in time using a direct N -body code. They derived that the initial properties of the parent cloud (mass, density) determine the characteristics of the emerging cluster, whether it will become an association, an open cluster or a dense massive one. Moreover, to form massive clusters, they claimed that a local SFE > 50 per cent is needed.

Using a more elaborate methodology, Dale & Bonnell (2011), Dale & Bonnell (2012), Dale et al. (2012b), Dale, Ercolano & Bonnell (2012a), Dale, Ercolano & Bonnell (2013a,b) studied in a series of papers the effects of photoionization FB on embedded clusters and its disruptive impact on clouds of different masses (from 10^4 to $10^6 M_{\odot}$) and sizes (from 2 to 220 pc), either initially bound or unbound. In Dale et al. (2014), the authors added stellar winds to photoionization FB and studied how the overall SFE, the average star formation rate (SFR) and the fraction of unbound gas varied with the initial cloud properties. Their methodology was based on SPH simulations of turbulent molecular clouds, with an initial shallow Gaussian density profile. The velocity field was initialized as a turbulent, divergence-free Gaussian random field, with a power spectrum to $P(k) \propto k^{-4}$ consistent with isothermal supersonic turbulence. The cloud was evolved using self-gravity and cooling, and star formation was modelled using sink particles. The mass and spatial resolution was also relatively low, with 10^6 particles per cloud, but using 100 neighbours in the smoothing kernel, so only 10^4 independent resolution elements (Dale, Bonnell & Whitworth 2007a). Radiative transfer of the photoionizing photons was performed using a Strömgren sphere filling technique (see Dale, Ercolano & Clarke 2007b, for details). Using the same set of simulations, Dale, Ercolano & Bonnell (2015) focused on the properties of the stellar populations of the star clusters formed. They found that the SFE is lowered by the presence of FB; however, they stressed how the disruptive effect of FB depends on the cloud properties, especially the escape velocity. Natal gas from massive clouds with elevated escape velocities is expelled only in minimal part. Winds are found to have little impact on the dynamics of gas compared to ionizing FB. Moreover, in these simulations the number of stars unbound by FB is very modest and is not related to the fraction of gas expelled.

Along the same lines as in Fujii & Portegies Zwart (2015), the longer term evolution of these star clusters was finally investigated in another series of paper by Parker & Dale (2013), Parker, Dale & Ercolano (2015) and Parker & Dale (2015). They concluded that clusters formed in simulations with FB tend to remain sub-structured longer than in the non-FB cases. Moreover, at the end of the pure N -body evolution, the authors found that

simulations with FB contain fewer bound stars than in the control run. In terms of mass segregation, they do not provide a unique conclusion, because different analysis return contrasting results.

More recently, several papers have addressed the problem of star cluster formation from a realistic, gaseous, turbulent environment using grid-based simulation techniques. Using the RAMSES code, Lee & Hennebelle (2016) studied the conditions required in the parent cloud to obtain a bound star cluster. The authors aimed to examine the properties of the gaseous proto-cluster born from the collapse of a $10^4 M_{\odot}$ molecular cloud. To achieve this, they performed magnetohydrodynamics simulations, without stellar FB and varying the initial level of turbulent support. Pre-stellar cores were followed using the same sink particles algorithm adopted in our work. The typical mass of a sink was $10 M_{\odot}$. The proto-cluster turned out to be in virial equilibrium, with turbulence and rotation supporting the collapse. The virial status and size of the proto-cluster were considered to be directly imprinted by the parent cloud; therefore, they concluded that the study of the gaseous proto-cluster phase is a fundamental step in the context of stellar cluster formation.

Using the FLASH code, coupled to a ray tracing code, Howard et al. (2016) studied the effect of various cloud initial conditions, then subjected to the ionizing radiation of massive stars, on the final properties of the star cluster system. This study focused on giant $10^6 M_{\odot}$ molecular clouds, with different initial virial parameters (α), ranging from bound ($\alpha = 0.5$) to unbound ($\alpha = 5$). The main goal was to study how FB and the virial status affect the formation of star clusters and subsequent evolution of the cloud. In this case, sink particles represented single star clusters and star formation within each cluster is implemented with a subgrid model, by randomly sampling the initial mass function (IMF). Their conclusion was that the initial virial parameter strongly influences the SFE, with more bound clouds having higher efficiency, while radiative FB did not play a major role, lowering the previous values only by a few per cent. They also found that the number of star clusters formed depends on the boundedness of the cloud: the more bound the cloud, the fewer the star clusters. Moreover, the clusters from unbound clouds were gas poorer and star richer than the ones formed from bound clouds.

In this work, we model the collapse of a $\sim 2.5 \times 10^4 M_{\odot}$ turbulent cloud with photoionization FB from massive stars at extremely high resolution (smallest cell size ~ 500 au), and study how the star cluster forms and emerges from its parent cloud. Our radiative transfer technique is based on the moment method with the M1 closure (Rosdahl et al. 2013) and allows us to model an arbitrary number of photon sources, much faster than traditional ray tracing schemes. We consider two different FB scenarios (strong and weak) and a reference simulation without any FB. We subsequently analyse how the different FB scenarios affect the properties of our newborn star clusters, using various observables related to the stellar mass function, its spatial distribution, the mass segregation, the distribution of escaping stars and the stellar multiplicity function.

The paper is organized as follows: in Section 2, we describe the numerical methods we have used for our simulations. In Section 3, we analyse the properties of the star clusters we have obtained, and finally, in Section 4, we discuss our findings in light of previous studies, both theoretical and observational.

2 NUMERICAL METHODS

We now describe in detail the numerical techniques we use to model the collapse of a turbulent molecular cloud and the formation of

massive stars, following the effects of ionizing radiation on the cloud itself.

2.1 Initial conditions

We first perform a decaying turbulence simulation in a periodic box sampled with 1024^3 cells. This simulation is initialized with a uniform gas density $\rho_0 = 1$ (in arbitrary units) and a Gaussian random velocity field with a power spectrum $P(k) \propto k^{-4}$, where k is the wavenumber. $P(k)$ is normalized so that the 3D velocity dispersion in the full box was set to $\sigma_{3D} = \mathcal{M}c_s$, where the sound speed is $c_s = 1$ in arbitrary units and the initial Mach number is set to $\mathcal{M} = 20$. After one turbulence crossing time, $t_{\text{turb}} = L/\sigma_{3D}$ (where the box size was also set to 1 in arbitrary units), the kinetic energy has decayed by a factor of 2, and the actual Mach number by a factor of $\sqrt{2}$. At that time, the turbulence is fully developed, with density fluctuations following a clear log-normal distribution function and the variance in $\log \rho$ reaching its peak value. Krumholz et al. (2012) found that whether turbulence is initially fully developed or not has significant impact on the results.

We then use this final snapshot as a template for the initial turbulent cloud. We first set up the physical scales of our problem. The cloud is considered to be fully composed of molecular gas hydrogen with temperature $T_0 = 10$ K and isothermal sound speed $c_s = 0.2 \text{ km s}^{-1}$. The mean density in the box is set to $n_H = 10^3 \text{ H cc}^{-1}$ and the periodic box length to 20 pc. We carve out of the periodic box a sphere of radius 5 pc, centred on a large filament resulting from a large compressive mode. As a result, the mean density in the spherical cloud is larger than the mean density in the original box, and the Mach number in the cloud is smaller than in the original box (by another factor of $\sqrt{2}$) with $\mathcal{M} \simeq 10$. The final cloud properties are the following: radius $R = 5$ pc, mass $M \simeq 2.5 \times 10^4 M_\odot$ and velocity dispersion $\sigma_{3D} \simeq 2 \text{ km s}^{-1}$. Note that, because we have adopted a velocity dispersion at the low end of values found in observations of clouds of a similar size, our cloud virial parameter

$$\alpha_{\text{vir}} = \frac{5\sigma_{3D}^2 R}{3GM} \simeq 0.3, \quad (1)$$

is small enough to ensure a fast collapse, i.e. the free-fall time is ~ 1 Myr. The simulations are then run to $t = 2$ Myr.

Such a choice for the virial parameter was meant to explore the stabilizing effect of FB. We chose, in fact, an extreme situation to investigate the action range of photoionization even in very bound and dense environments, characterized by a high degree of dynamical interactions and escaping stars. Moreover, cloud disruption driven by large-scale turbulence (see works by Dale et al.) is not effective for our cloud. We intend to relax such an extreme condition in a follow-up paper.

2.2 Refinement strategy

Our initial coarse grid corresponds to a minimum refinement level $\ell_{\text{min}} = 10$ with cell size $\Delta x_{\text{max}} \simeq 0.02 \text{ pc}$, which allows us to resolve our sonic scale $l_s \simeq 0.08 \text{ pc}$, i.e. the scale at which our scale-dependent 3D velocity dispersion is equal to the sound speed. During the course of the simulation, we refine this initial grid level using a quasi-Lagrangian refinement criterion. Our maximum resolution is fixed to our maximum refinement level $\ell_{\text{max}} = 13$, which corresponds to a minimum cell size of $\Delta x_{\text{min}} \simeq 500 \text{ au}$. Assuming

for the isothermal sound speed $c_s = 0.2 \text{ km s}^{-1}$, and requiring for the Jeans length

$$\lambda_J = c_s \sqrt{\frac{\pi}{G\rho}} > 4\Delta x_{\text{min}}, \quad (2)$$

this gives us the constraint that $\rho < \rho_J \simeq 2 \times 10^{-17} \text{ g cc}^{-1}$. This maximum density corresponds also to a Jeans mass

$$m_J = \frac{4\pi}{3} \rho_J \left(\frac{\lambda_J}{2}\right)^3 \simeq 0.14 M_\odot. \quad (3)$$

We require to resolve this Jeans mass with at least 64 resolution elements, which gives us a mass resolution of $m_{\text{res}} \simeq 2 \times 10^{-3} M_\odot$. Our refinement strategy is thus the following: if a cell has accumulated a gas mass larger than m_{res} , then it is refined individually into eight new children cells, up to the maximum refinement level. Note that with our adopted initial coarse level and our quasi-Lagrangian strategy, we also automatically satisfy the additional criterion that the Jeans length is always refined by at least four cells for any gas density smaller than ρ_J .

2.3 Sink particles

When the gas density exceeds ρ_J , we violate our requirement to always resolve the Jeans length with four cells and the Jeans mass with 64 resolution elements. Therefore we adopt this criterion to form sink particles, using the technique developed in Bleuler & Teyssier (2014). We first detect density peaks in our 3D density field using the PHEW* clump finder (Bleuler et al. 2015). The density threshold is set to $\rho_{\text{threshold}} = 2 \times 10^{-18} \text{ g cc}^{-1}$, or 10 percent of the Jeans density. After we have identified a discrete set of peak patches delimited by either the isosurface at the density threshold or the saddle surface with a neighbouring peak patch, we draw a sphere, four-cell size in radius, around the density maximum. If the density at the maximum exceeds the Jeans density, if the sphere is contracting and if its virial parameter is less than 1, we form a sink with a seed mass equal to $m_J \simeq 0.14 M_\odot$ (see Bleuler & Teyssier 2014, for details). In our simulations, one sink corresponds to a single star.

The sink particle is then treated like a point mass. We follow the sink particle dynamics by a leap-frog, direct N -body integrator, using a softened $1/r^2$ acceleration (with softening length $0.5\Delta x_{\text{min}}$) between sinks, and also between the sinks and the gas. Only the self-gravity of the gas is based on the grid-based Poisson solver in RAMSES. Gas accretion on to the sink particles is modelled through what is described as ‘flux accretion’ in Bleuler & Teyssier (2014).

2.4 Radiative processes

In this paper, we model the emission and the propagation of ionizing, UV radiation, together with associated heating and cooling processes. We used the RAMSES-RT radiative transfer module developed by Rosdahl et al. (2013), using one photon group, with energies between 13.6 and 24.6 eV. We do not account for photon energies below 13.6 eV, namely optical and infrared radiation, as the scope of the paper is to study the effect of photoionization heating on the molecular cloud. We will study these other sources of radiation in a follow-up paper. Details in the adopted photoabsorption cross-section, chemistry and cooling processes are available in Rosdahl et al. (2013). Metal cooling prescriptions are based on Sutherland & Dopita (1993) for temperatures above 10^4 K and on Rosen & Bregman (1995) for metal fine-structure cooling below 10^4 K. We

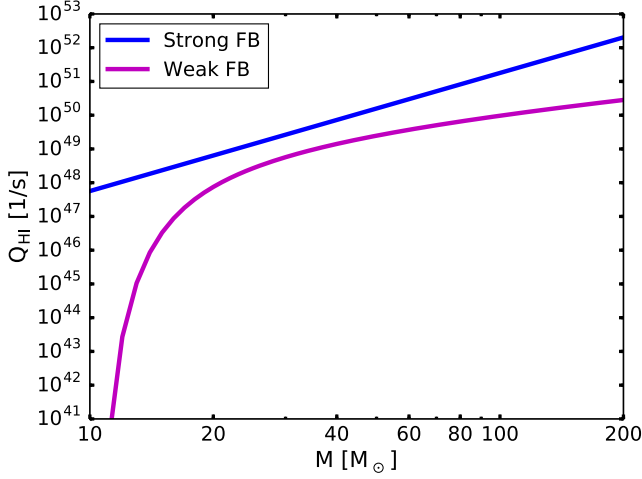


Figure 1. Number of emitted ionizing photons per second as a function of stellar mass.

extended the cooling function by Rosen & Bregman (1995) down to 10 K, to account for CO and fine structure cooling due to C II, O I, according to prescriptions of Dalgarno & McCray (1972). Following Geen et al. (2015, 2016), the photon group energy and cross-section are derived sampling the blackbody spectral energy distribution of a $20 M_{\odot}$ star. The frequency-dependent ionization cross-sections are taken from Verner et al. (1996) and Hui & Gnedin (1997). A reduced speed of light of $10^{-4} c$ is used. This is done to improve the efficiency of our simulations, since the speed of light affects the timestepping calculation, through the Courant factor.

The UV radiation emitted by the sink particles is modelled using the following simple strategy. We implemented two FB regimes, namely *strong* and *weak*. For the strong FB case, we basically consider all the energy emitted from the sink/star (even optical and infrared) as ionizing radiation. To derive the energy associated with every sink we assume a power-law luminosity–mass relation, $L = L_{\odot} (M/M_{\odot})^{3.5}$, where L_{\odot} and M_{\odot} are the solar luminosity and solar mass, respectively. The number of photons emitted per second, Q_{HI} , was then obtained by dividing this luminosity by a mean value of photon energy in the ionization range (13.6–24.6 eV).

For the weak FB case, we computed an analytical fit of photon emission rates presented in Sternberg, Hoffmann & Pauldrach (2003), obtained through radiation-driven wind atmosphere models of OB stars. We derived the following analytic expression of the number of emitted ionizing photons per second as a function of the stellar mass:

$$\log[Q_{\text{HI}}(M)] = 48.65 + \log(M/M_{\odot}) - \frac{2.4}{\log(M/M_{\odot} - 8)^{1.9}} \cdot (4)$$

This formula was applied to calculate emission rates for all sinks with $M > 10 M_{\odot}$. For stars with lower mass, we assume there are no ionizing photons. Fig. 1 compares the resulting Q_{HI} from the two FB models considered.

3 ANALYSIS

In this section, we focus on the analysis of the simulations. In particular, we study the structural characteristics of the star cluster (such as mass function, virial status, mass segregation, escapers, binaries) in the three different runs, to understand the role of FB in shaping the star cluster itself.

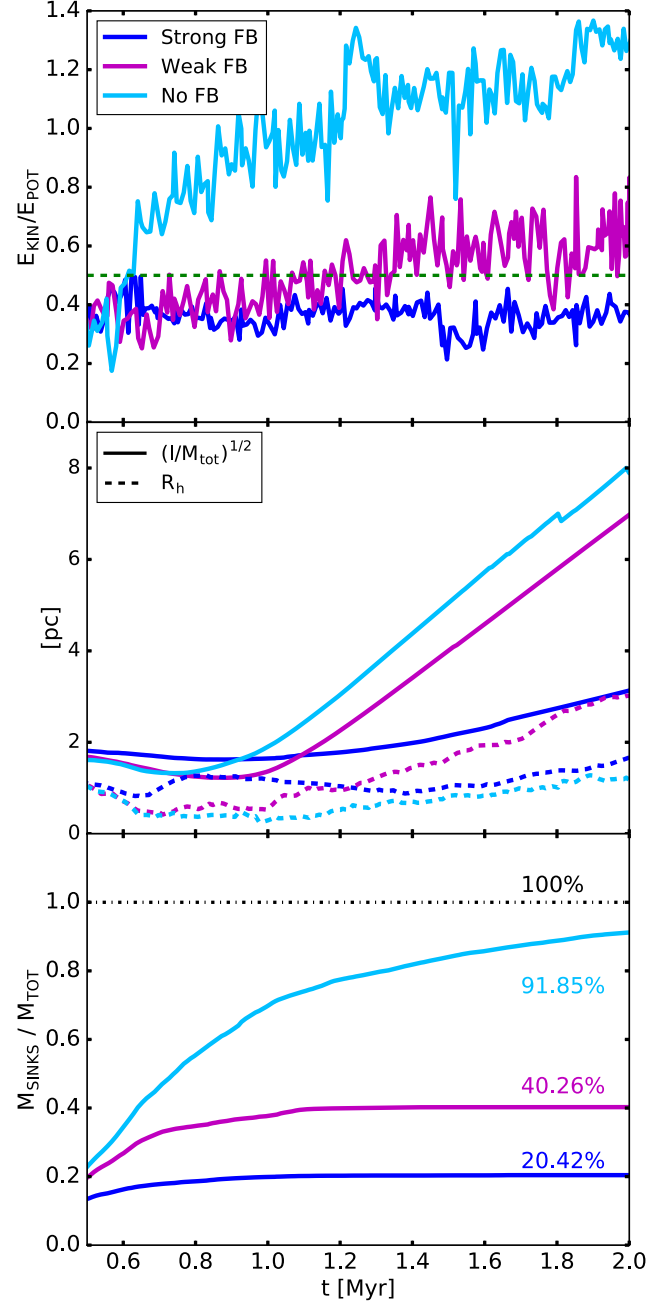


Figure 2. Top panel: ratio of total kinetic to potential energy of the sinks (virial ratio, E_k/E_p), the dashed green line indicates the virial equilibrium. Middle panel: size of the star cluster, in terms of half-mass radius (dashed line) and moment of inertia-derived radius (solid line). I and M_{SINKS} indicate respectively the moment of inertia and total mass of sinks. Bottom panel: SFE evolution with time computed as the mass fraction in sinks (M_{SINKS} indicates the total mass in sinks, M_{TOT} , the total initial mass of the gas cloud). The ionizing radiation suppresses the formation of stars by clearing gas out of the cloud, and it increases the virial stability of the emerging star cluster.

Fig. 2 shows ratios of kinetic to potential energies of sinks (upper panel), cluster sizes and the SFE (lower panel) as a function of time. Focusing first on the SFE, the ionizing radiation clearly has a major effect in suppressing star formation. In Figs 3 and 4, we demonstrate the effects of the radiation qualitatively, plotting time-sequences of

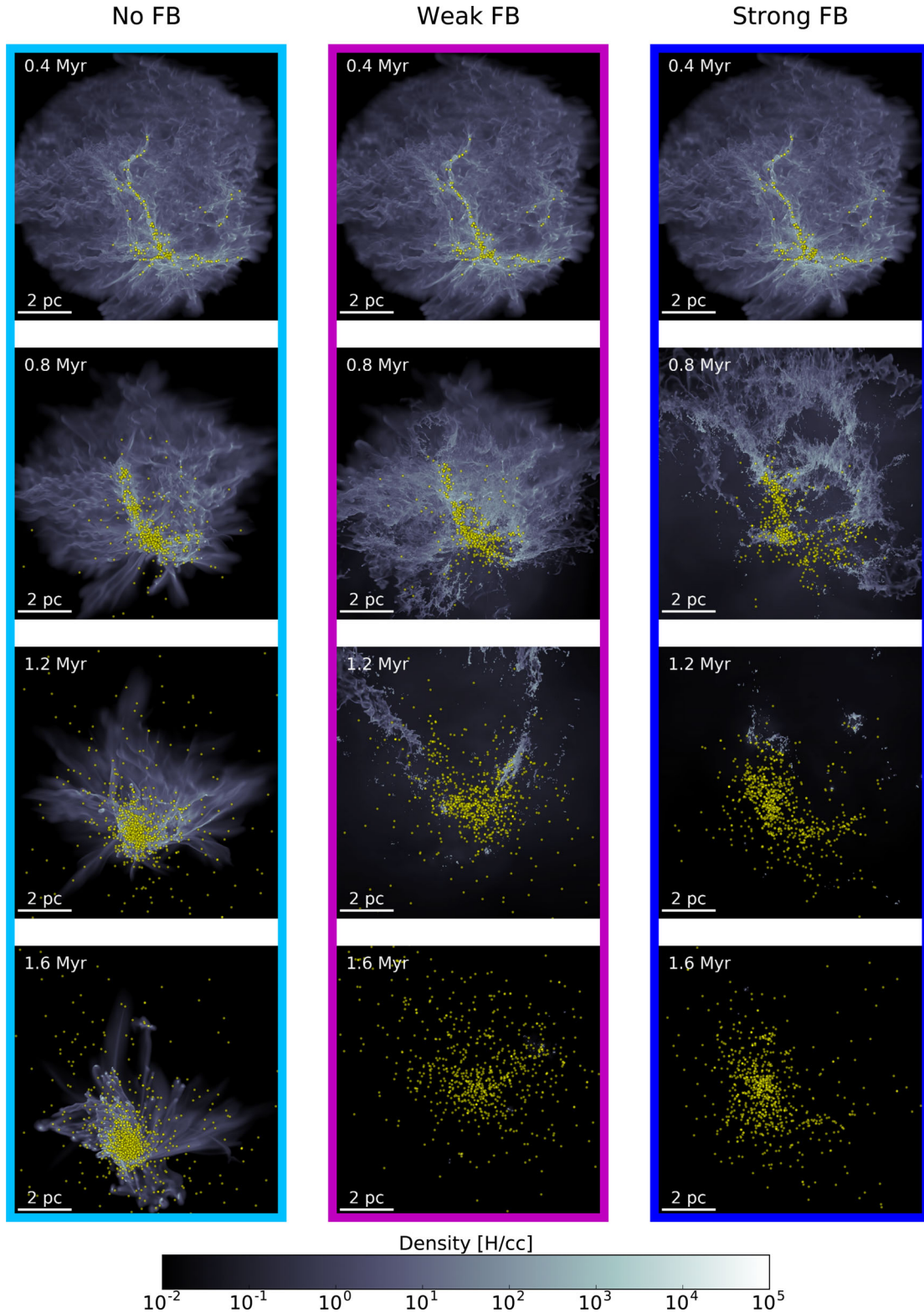


Figure 3. Mass-weighted line-of-sight projections of gas density for all three runs at different times. The strong FB case is in always denoted with dark blue colour, weak FB case with magenta and the run without FB with azure. Sink particles are indicated in yellow.

gas density and temperature maps, to compare the strong, weak and no-FB cases. The initial phase of the cloud collapse proceeds identically in the three cases. The cloud gravitationally contracts and starts forming filaments, where local overdensities allow the

creation of stars, here represented by sinks (in yellow or turquoise, depending on the map).

In the no-FB case this contraction proceeds without resistance until eventually all the gas is converted into stellar objects; from Fig. 3

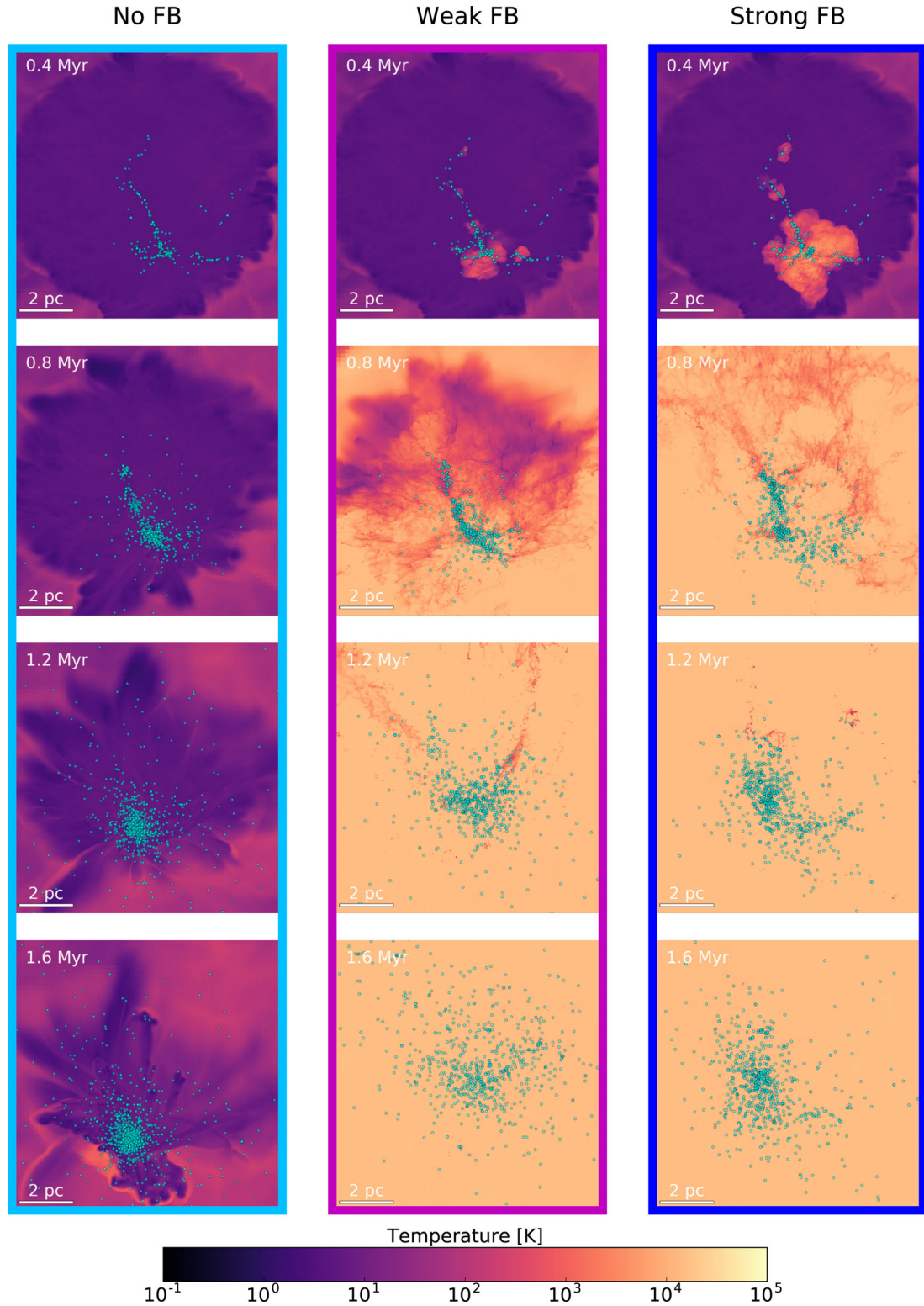


Figure 4. Mass-weighted line-of-sight projections of gas temperature for all three runs (strong, weak and no FB) at different times. Sink particles are indicated in turquoise.

we can see how even in the latest snapshot the amount of dense gas is still high and by the end of the simulation time (2 Myr) the fraction of total mass still available in gas is ~ 10 per cent. In general, we can notice how the final shape of the star cluster becomes more and more spherical with the simulation progressing. The gas

temperature in the no-FB case does not show huge changes throughout the collapse.

In the weak-FB case, stars emit ionizing radiation and we now follow the photochemistry of hydrogen. Differences with the no-FB case start being visible around already 0.4 Myr in the temperature

map, when the most massive stars in the lower part of the filament start emitting UV photons and cause the gas temperature to increase locally. This bubble of hot gas becomes more and more extended since more stars are formed, accreting more gas. The neutral H I gets dissipated, due to the quick expansion of the H II region. At the end of the simulation, the star cluster is completely free of dense and neutral gas. The strong-FB case is analogous to the weak-FB case but the process of photoionization and gas expulsion is much more rapid and violent, so as a result the star cluster is devoid of gas already at 1.2 Myr.

3.1 Virial properties

In the top panel of Fig. 2 we show the evolution over time of the virial ratio of the star cluster, E_k/E_p (where E_k and E_p are respectively the total kinetic and potential energy of the sinks) for the three simulations. We do not consider snapshots before 0.5 Myr because before this time there is still a large amount of gas mass which will become sinks, and therefore the stellar cluster cannot yet be treated as isolated system.

As seen in the figure, the case without FB is clearly supervirial, hence expanding. The two cases with FB, instead, result in virial or even sub-virial state. This can be explained as a result of FB, which halted the collapse of the cloud, ionizing and dispersing the neutral gas. This determined the formation of a much less dense aggregation of stars than in the control simulation. In the run without FB, the collapse proceeds unhindered and the newborn stars are immersed in a dense, highly collisional environment, experiencing very strong close interactions. This inevitably leads to the ejections of many sinks and expansion of the cluster. The middle panel of Fig. 2 clarifies the evolution of the size of the star cluster, considering both the half-mass radius (dashed line) and the global size obtained as $\sqrt{I/M}$, where I is the moment of inertia of the cluster and M is the total mass. From the plot it can be seen that the reference run is the more extended one, but at the same time half of its mass is very concentrated at the centre. The expansion is then due to the escaping (massive) stars, not to a generally unbound cluster (a similar case was presented in Kuznetsova, Hartmann & Ballesteros-Paredes 2015). However, when FB is included, its effect is to oppose this runaway collapse and allow the onset of a lower density regime, where the stellar distribution finds a stable configuration.

It is interesting to notice how this result goes against traditional predictions (see the Introduction), which argue for a complete disintegration of the star cluster after a violent expulsion of gas. However, these often assume a fully formed star cluster still embedded in gas, which at some point gets ejected. In our case, stars are created while the gas is expelled in a self-regulating fashion. Therefore the virial status of the emerging star cluster changes along with the collapse. The outcome of our simulations results from the interplay between the highly subvirial initial virial ratio and the strength of the FB adopted: a very subvirial cloud produces a cluster too dense to survive, unless FB slows down the collapse. We also conclude that the SFE alone is not a good indicator of the survivability, as it is usually believed.

In the lower part of Fig. 2 we show the fraction of gas transformed into stars. Stellar FB is very efficient in stopping the collapse and lowering the SFE. In fact in the case with the strongest FB the SFE halts at ~ 20 per cent (while virtually unity for the control simulation). For a weaker FB, we get a higher fraction. Despite the fact that in the simulation without FB all gas is eventually transformed into stars, we stress that the outcome of the simulation is the dispersal of the emerging star cluster, while for the strong FB

case, which results in a very low SFE, the outcome is a stable (or even subvirial) star cluster.

3.2 Mass function

In Fig. 5, we plot the stellar mass function for all the FB cases we have considered and at different times. In the run without FB, our mass function peaks at a relatively large mass of $\sim 10 M_\odot$ and shows a strong accumulation of very massive stars at the high-mass end, with the mean sink mass being around $15 M_\odot$ and the most massive sink reaching $460 M_\odot$. This is due partly to our limited resolution (see later) and to the lack of FB to limit the maximum stellar mass. In the weak FB scenario, the maximum mass is lower, around $250 M_\odot$ and the mass function flattens, with a slight increase of very low mass stars (close to our resolution limit of $0.1 M_\odot$). The trend gets even clearer if we look at the case with strong FB, where there is a significant peak of stars with mass around $0.1 M_\odot$ (corresponding to the sink seed mass) and the most massive star is now around $120 M_\odot$. We observe in the simulation that this excess of low-mass stars close to the resolution limit is caused by the fragmentation of the outer dense shells of H II regions.

Looking at the mass function at earlier times (specifically, $t = 0.25$ Myr and $t = 0.5$ Myr, paler lines in Fig. 3), it is clear that the onset of the sink mass function proceeds similarly in the three cases. It is mainly the final mass distribution that shows visible differences between the FB and no-FB cases. To summarize, these are (1) the high-mass cut-off due to FB effects that stop accretion on to massive sinks, (2) a peak at the low-mass end, due to fragmentation of dense gas around H II regions.

3.2.1 Comparison to observations

It is very instructive to compare the results of our simulations to available observations. We choose to consider NGC 3603 YC and the Arches cluster, since they are among the youngest (< 2 Myr) well-studied star clusters, part of large, still gas-rich, regions.

NGC 3603 YC (also known as HD 97950) is a very compact and massive young star cluster at the centre of the vast homonym H II region. It is composed of three Wolf-Rayet stars and around 40 O-type stars, a dozen of which reside in the very central part of the core, less than 1 ly from the centre (Drissen et al. 1995). Harayama, Eisenhauer & Martins (2008) estimated the total mass to be between 1 and $2 \times 10^4 M_\odot$. The H-R diagram in Melena et al. (2008) reveals the presence of at least 15 stars with masses greater than $60 M_\odot$. The most massive stars in the cluster seem to be coeval with ages between 1 and 2 Myr (Stolte et al. 2004; Melena et al. 2008; Kudryavtseva et al. 2012). However, the age spread between the pre-main-sequence stars (Beccari et al. 2010) and the slightly older stars in the cluster outskirts (Sung & Bessell 2004) suggests a possible extended star formation scenario.

The Arches cluster is considered to be the densest cluster in our Galaxy. It also falls in the category of so-called starburst star clusters. It is located near the Galactic Centre and its age is estimated to be around 2 Myr. Its total mass is estimated to be around $2 \times 10^4 M_\odot$ (Espinoza, Selman & Melnick 2009) and it contains 160 O-stars and 13 Wolf-Rayet¹ (Figer 2004; Martins et al. 2008).

¹ This is about 5 per cent of all known Wolf-Rayet stars in the Milky Way (Figer et al. 2002).

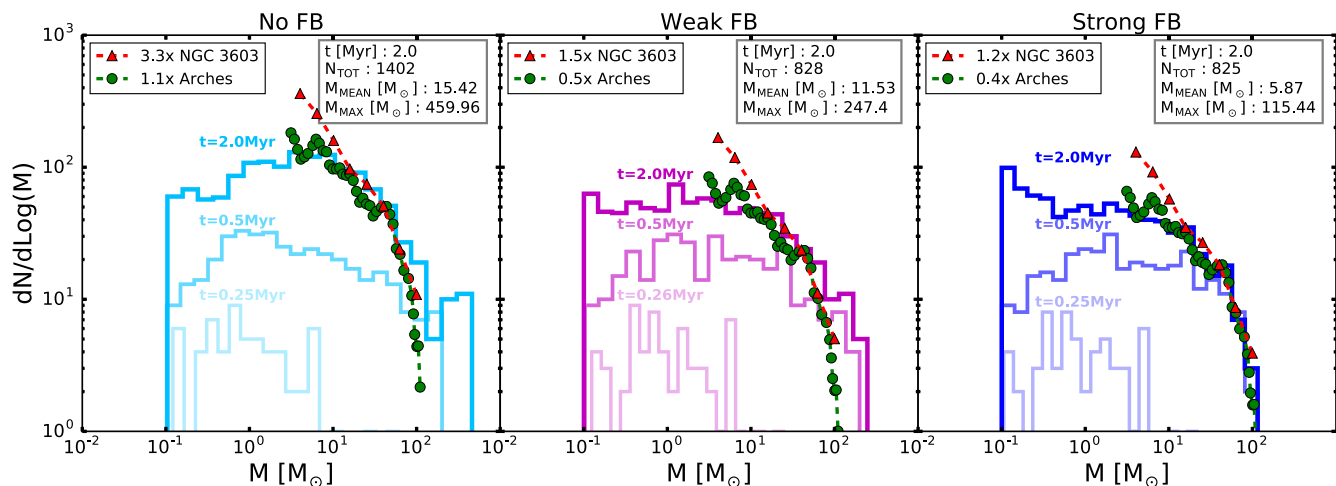


Figure 5. Mass function profile for all three feedback regimes. The thicker and darker lines indicate for every run the mass function profile at $t = 2$ Myr. In the top right box of every subplot, we indicated the total number of sinks, the average and maximum sink masses at $t = 2$ Myr. In every subplot, we plot also the mass functions at $t = 0.5$ Myr and $t = 0.25$ Myr in paler colours. The green dots correspond to the normalized observational data for the Arches cluster (Stolte et al. 2005), the red triangles the same for NGC 3603 (Pang et al. 2013). The normalization factors are reported in the top left box. Our strong feedback case compares best with the normalized observations, although all models fail to reproduce the steep curve towards lower masses in NGC 3603.

For NGC 3603 YC, we considered the mass function results published by Pang et al. (2013) and for the Arches the one published by Stolte et al. (2005). To derive the mass function of NGC 3603 YC, the authors considered stars in absolute V -magnitude bins and then derived the correspondent masses using the isochrone models from Lejeune & Schaerer (2001) for high-mass stars and Siess, Dufour & Forestini (2000) for low-mass stars. Their mass bins have a logarithmic size of 0.2. The data were corrected both for incompleteness and foreground stars contamination and include all stars within 60 arcsec (~ 2 pc).

Stolte et al. (2005) derived the present-day mass function of the Arches cluster by converting the K -band magnitudes from the corrected colour–magnitude diagram into masses using a 2 Myr Geneva main-sequence solar metallicity isochrone from Lejeune & Schaerer (2001). They also binned their data using logarithmic intervals of size 0.2 and they computed the mass function 10 times, each time shifting the bins by 0.02. The final present-day mass function was created by averaging all the points from these 10 mass functions and takes into account all stars within 0.4 pc.

Comparing these observational data to our simulations is not trivial, since we do not know the SFE of the parent clouds of both NGC 3603 YC and the Arches. The targeted clusters have about twice the mass of our simulated ones from the FB runs, but roughly equal to the one in our no-FB simulation. If the true SFEs of the observed star clusters were very low, say 10 per cent, this would imply that the original clouds would be as massive as $10^5 M_\odot$, which is computationally too expensive to simulate at the current resolution and with our radiation solver. Therefore, we decided to renormalize the observations. The normalization factors are computed requiring that the mass bin at $15 M_\odot$ in the two observational data sets have the same value, equal to that of our simulated data set. The normalization coefficients for the Arches data set are 0.4, 0.5 and 1.1 with respect to the strong, weak and no-FB cases, respectively, while the normalization coefficients for the NGC 3603 data set are 1.2, 1.5 and 3.3 with respect to the strong, weak and no-FB cases, respectively.

In Fig. 5 we compare these renormalized observed mass functions to our simulated ones. Renormalized observational data are showed

with red triangles (NGC 3603) and green circles (Arches). The best agreement, especially at the high-mass end, is obtained with the strong FB (after renormalization). The weak and no-FB runs clearly produce too many very high-mass stars. The agreement is worse at lower masses, especially below $10 M_\odot$. As we explain below, we believe this is due to our limited resolution.

3.2.2 Slope of the mass function

The previous analysis was carried out considering all the sinks in the simulation box. We now study the mass function dependence with radius. In Fig. 6, we show the mass function taking into account only sinks within specific radii,² namely 1, 3 and 5 pc, and for all three FB regimes. The last radial bin contains 92 per cent, 74 per cent and 88 per cent of the simulated sinks respectively for strong, weak and no FB. The solid curve corresponds to the whole box, or a radius of 10 pc. Although the mass function appears to be independent of radius for the no-FB case, it looks clearly flatter in the inner parts and steeper in the outer parts for the two FB cases. Pang et al. (2013) showed that a similar effect is present in NGC 3603: the slope of the mass function steepens with radius, indicating that the most massive stars are mostly concentrated in the centre. This feature is generally explained by mass segregation. We will develop this topic in the next section.

If we now quantify the slope of the mass function, we found that all our simulations show a slope (Γ) much flatter than that of the Salpeter IMF (i.e. $\Gamma = -1.35$), depending sensitively on the range of masses used to compute it (see Fig. 6), which means the mass function is probably not a power law all in all. A shallower slope than the Salpeter is also the case for observed young and embedded star clusters. NGC 3603, for example, has $\Gamma = -0.88 \pm 0.15$, considering only $\log(M/M_\odot) > 0.6$ for completeness reason. For the Arches, Stolte et al. (2005) detected a change in the slope of the mass function at about $6 M_\odot$; hence, they fitted the mass function

² Unless otherwise stated, the radius is always considered respect to the centre of density of the system defined as in Portegies Zwart et al. (2001).

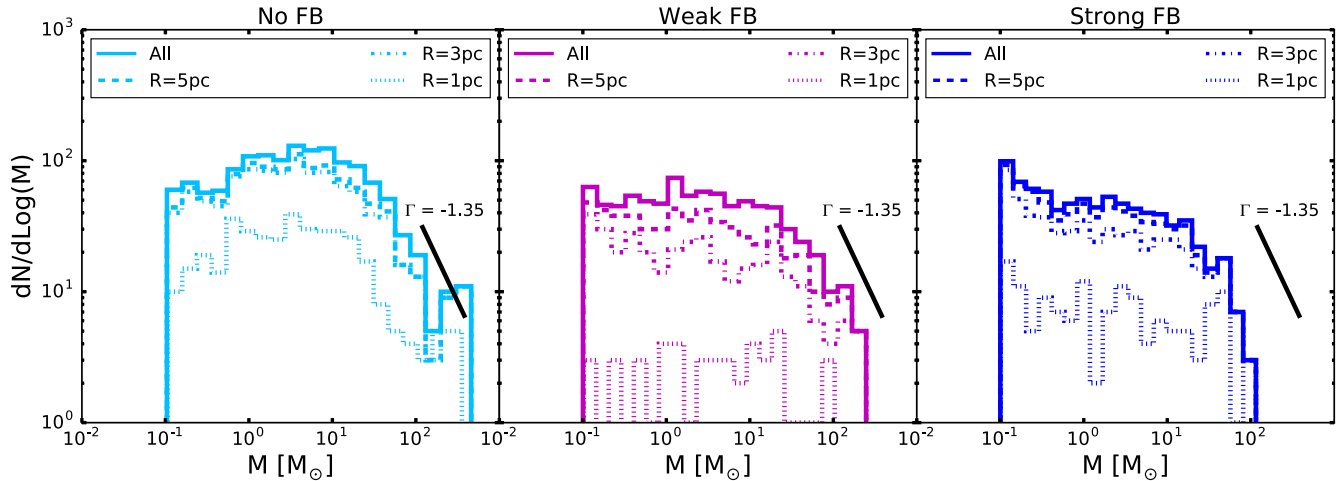


Figure 6. Mass functions at different radii, $R = 1, 3$ and 5 pc. The solid thick line refers to the total mass function (all sinks included). In black the Salpeter slope ($\Gamma = -1.35$) is indicated as a reference. In all cases, the slope of the simulated mass functions is flatter than the Salpeter one. Moreover, the slope steepens with radius, especially in the FB cases, indicating a higher concentration of massive stars in the centre.

in the range $\log(M/M_\odot) > 0.8$. The resulting value was measured to be $\Gamma = -0.86 \pm 0.15$. Both these clusters have slopes flatter than the Salpeter slope, which seems to be in general a distinguishing feature of young starburst clusters.

The origin of this discrepancy from the Salpeter slope is probably due to many reasons. On the simulation side, Bertelli Motta et al. (2016) showed that the simulated IMF can be affected by resolution, with the peak or turn-over mass depending directly on it. The higher the resolution, the lower the turn-over mass, which implies a progressive steepening of the mass function with increasing resolution. These authors estimated that the peak mass is roughly ~ 30 times the minimum Jeans mass, which in our case corresponds to about $4.5 M_\odot$, and agrees quite well with our no-FB case. Studying the formation of low-mass protostars in radiative FB simulations, Bate (2014) obtained IMF profiles with slopes compatible with the Salpeter prescription.

So, resolution effects are likely a cause of the low value for Γ in our simulations in the intermediate mass range $\log(M/M_\odot) < 1$. Moreover, FB inevitably plays a role in all this, lowering the number of stars in the intermediate–high-mass range, therefore contributing to an even shallower slope. At larger masses, on the other hand, recent theories of turbulent cloud collapse argue for an asymptotic Salpeter slope (Hennebelle & Chabrier 2008; Hopkins 2012). This could be consistent with our simulated star clusters, but also with the observed ones, without being very conclusive, reminding us that the story is probably not so simple.

3.3 Mass segregation

We have already introduced mass segregation in the previous section to explain a steepening of the slope of the mass function as a function of radius. We now analyse our simulations with more traditional tools to quantify mass segregation in star clusters. A star cluster is considered to be mass segregated when the massive stars are more centrally concentrated than the lower mass stars. The main question related with mass segregation is whether it has a primordial or a dynamical origin. Mass segregation can indeed be the result of two or three body interactions between stars (dynamical) or the direct outcome of the star formation process within the gas cloud

itself (primordial). Our simulations are ideal experiments to try and answer this question.

The problem of comparing the mass function for different radii to characterize mass segregation is that we need to define unambiguously the centre of the star cluster, which is a difficult task. Allison et al. (2009) introduced the Minimum Spanning Tree (MST) to quantify the degree of mass segregation in a star cluster. The MST is defined as the shortest path connecting all points, which does not contain any closed loop. We used the routine included in the `csgraph` module of `SCIPY`, which implements the MST according to Kruskal’s algorithm (Kruskal 1956).

We followed Allison et al. (2009) prescription to quantify mass segregation using the MST. We computed the length, L_{massive} , of the MST of the N most massive stars and compared this to the average length of the MST of N random stars in the cluster, or L_{random} . L_{random} was calculated by picking 1000 random sets of N stars, in order to have a small error on the dispersion σ . Mass segregation is quantified using the *Minimum Spanning Tree Ratio* Λ_{MSTR} defined by Allison et al. (2009) as

$$\Lambda_{\text{MSTR}} = \frac{L_{\text{random}}}{L_{\text{massive}}} \pm \frac{\sigma}{L_{\text{massive}}}.$$

For $\Lambda_{\text{MSTR}} \sim 1$, the distribution of massive stars is comparable to that of all stars. For $\Lambda_{\text{MSTR}} > 1$, massive stars are more concentrated, a clear sign of mass segregation. The larger Λ_{MSTR} , the more pronounced is the mass segregation.

This method was already adopted by Parker et al. (2014, 2015) to analyse the dynamical evolution of star-forming regions, starting from the final states of the SPH simulations by Dale et al. (2012b,a). Using Λ_{MSTR} for their $N = 10$ most massive stars, they found in their no-FB simulation a strong primordial mass segregation with $\Lambda_{\text{MSTR}} \simeq 5$, which disappears after 3 Myr due to stellar evolution and reappears at the same level after 8 Myr due to dynamical interactions between the cluster members. However, in their FB simulations that include winds and photoionization, they did not detect any mass segregation, with $\Lambda_{\text{MSTR}} \simeq 1$ at all times.

In Fig. 7, we plot Λ_{MSTR} as a function of N_{MST} , the number of stars we use for the spanning tree, at $t = 2$ Myr. We include in our analysis all stars up to an outer radius of 7.7, 9.3 and 9.8 pc, corresponding to the distance from the centre of the cluster of the most external bound star, in the strong, weak and no-FB cases, respectively. This is done

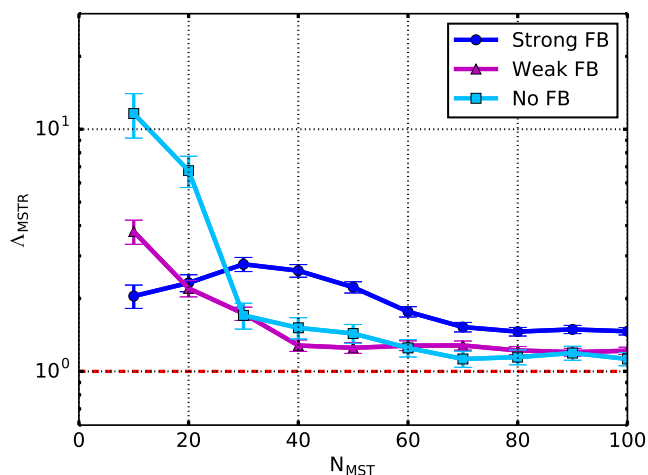


Figure 7. Minimum spanning tree ratio Δ_{MSTR} against number of stars used to calculate the length of the tree. The red dashed horizontal line indicate the value $\Delta_{\text{MSTR}} = 1$, meaning no mass segregation. The vertical bars correspond to 1σ error of Δ_{MSTR} . All three cases show some degree of mass segregation.

to prevent extreme outlier stars from dominating the calculation of the random spanning tree. Our data point with $N = 10$ corresponds to the estimator used in Parker et al. (2015).

All three cases show some degree of mass segregation. Our no-FB case is strongly mass segregated for $N = 10$ with $\Delta_{\text{MSTR}} \simeq 10$, and is still significantly segregated for $N = 20$ with $\Delta_{\text{MSTR}} \simeq 5$. The signal however disappears for $N \geq 30$. The strong FB case shows the weakest mass segregation for $N = 10$ with $\Delta_{\text{MSTR}} \simeq 2$, but the segregation signal is still detectable up to $N = 60$. The weak FB case lies in between the two other cases.

The two crucial pieces of information Fig. 7 provides are (1) the degree of mass segregation of the cluster, namely the value of Δ_{MSTR} and (2) the extent of mass segregation, namely the maximum number of stars that are mass segregated. From our results, two different situations emerge. In the no-FB case (and to some extent in the weak FB case), only a handful of supermassive stars are tightly concentrated at the centre. Only those most massive stars are mass segregated. The high stellar density is supported by the high measured values of Δ_{MSTR} . This population of massive stars forms effectively a sub-cluster at the centre of the main cluster, that keeps contracting and decouples dynamically from the rest, transferring its kinetic energy to less massive stars that are ejected (see next Section).

On the contrary, in the strong FB case, photoionization FB is efficient enough to halt the collapse of the gas, limiting the number density of massive stars. This prevents the formation of an independent self-gravitating system within the cluster itself. This translates into a lower degree of mass segregation and at the same time a higher number of stars being mass segregated.

In order to compare with observations, we plot Δ_{MSTR} as a function of the stellar mass (Fig. 8). Following Pang et al. (2013), we sort the stars by their mass and then consider blocks of 20 stars moving in steps of 10 stars, such that the data partially overlap. For example, the first 20 stars in the weak FB case (magenta line in Fig. 8) cover the range 200 to 80 M_{\odot} in mass, the second mass group goes from 130 to 60 M_{\odot} , etc. The mass interval considered is indicated by horizontal bars in the plot. For every bar a marker denotes the mean mass of the interval.

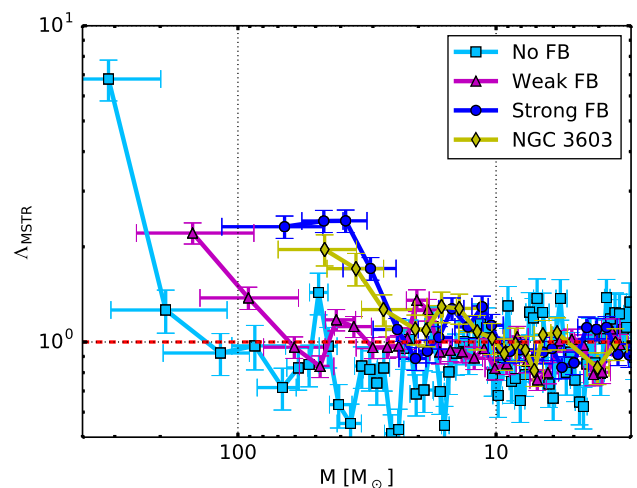


Figure 8. Minimum spanning tree ratio Δ_{MSTR} versus stellar mass. The red dashed horizontal line indicates the value $\Delta_{\text{MSTR}} = 1$, meaning no mass segregation. The vertical bar corresponds to 1σ error of Δ_{MSTR} . Horizontal bars show the mass interval covered by every group of 20 stars. Note that the horizontal line associated to the first data point for the non-FB case extends to the left until $\sim 400 M_{\odot}$. Observations are indicated in yellow. All curves show a similar behaviour, even if shifted towards higher masses. The best agreement with observations is provided by the strong FB simulation.

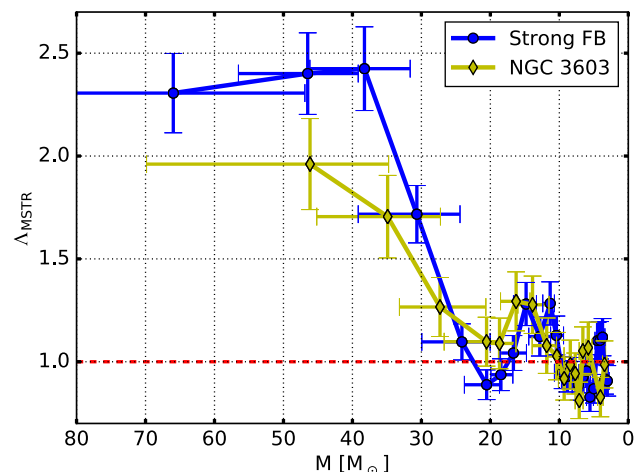


Figure 9. Zoom-in plot of Fig. 8. The comparison here is only between strong FB case and NGC 3603 YC.

The three profiles of Δ_{MSTR} versus mass in Fig. 8 look qualitatively similar, but they are shifted to higher and higher masses with increasing FB strength. The no-FB case shows mass segregation only in the first bin ($M > 200 M_{\odot}$) with an amplitude much larger than unity. For the weak FB case, only stars down to a mass of 60 M_{\odot} are weakly segregated, with an amplitude of 2, and for the strong FB case, the transition goes down to 30 M_{\odot} .

In Fig. 8, we compare our simulations to the data of Pang et al. (2013) on NGC 3603 (yellow points). A very good agreement is obtained with the strong FB case. In Fig. 9, we plot only the strong FB case and the observations using a linear scale in mass to allow a better comparison and to outline the very good quantitative match between our model and the observed segregation, both in terms of amplitude and of transition mass.

Despite being young, NGC 3603 shows already a clear signal of mass segregation. This is not an isolated case. There is also strong

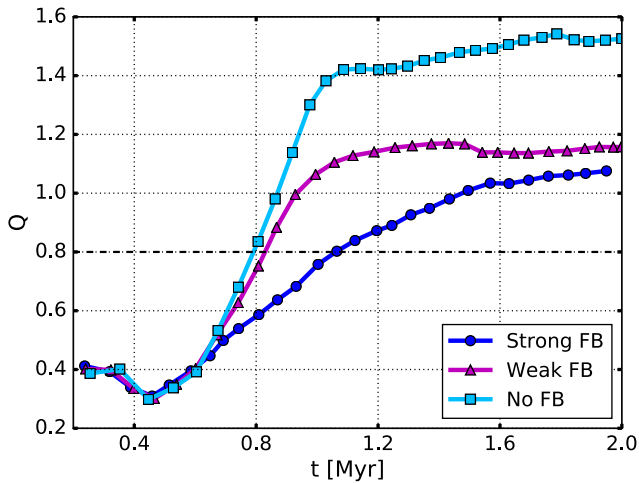


Figure 10. Evolution with time of the Q parameter. The dashed horizontal line corresponds to $Q = 0.8$. This value discriminates between centrally concentrated (>0.8) and fractal (<0.8) spatial configuration. The simulations with FB preserve substructures longer than the control run.

evidence of mass segregation in the Orion nebula clusters, but also in the Arches, NGC 6611, NGC 2244 and NGC 6530, to name a few (Hillenbrand & Hartmann 1998; Stolte et al. 2002; Bonatto, Santos & Bica 2006; Schilbach et al. 2006; Chen, de Grijs & Zhao 2007). The origin of the mass segregation in these clusters is still an open question (primordial or dynamical).

Pang et al. (2013) proposes for NGC 3603 a dynamical origin. Using analytical arguments, they show that the cluster dense core could dynamically segregate in one crossing time down to a mass of $30 M_{\odot}$. To test this hypothesis, we have performed our clustering analysis at earlier times and find no indication of mass segregation for massive stars. We have estimated the local two-body relaxation time-scale of the densest part of the cluster ($r < 2$ pc) and find it to be less than 0.5 Myr for all three cases, supporting our claim that dynamical friction can cause mass segregation after 1 Myr.

To quantify further the structure and morphology of our star clusters, we have used another statistical indicator called the Q parameter (Cartwright & Whitworth 2004). Q is defined as the ratio between the normalized mean edge length \bar{m} of the MST of all stars in the cluster and the normalized correlation length \bar{s} of the same stars.³ These parameters taken separately cannot distinguish between a smooth, radially concentrated distribution and an extended, fractal distribution, but their ratio can (Cartwright & Whitworth 2004). A cluster with $Q > 0.8$ is smooth and centrally concentrated, while if $Q < 0.8$, it is extended with a fractal distribution.

In Fig. 10, we show the evolution of the Q parameter with time. In all our simulations, the star cluster is initially fragmented and extended. The no-FB case rapidly evolves towards a more spherical and centrally concentrated distribution with $Q \simeq 1.5$, while in the two other cases, the transition is slightly slower, supporting a longer survival of substructures, and reaches a smaller maximum value with $Q \simeq 1.1$ and 1.2. This supports a scenario in which gravitational collapse together with stellar dynamical interactions progressively erase the initial conditions in the gas cloud and build up a dense and spherical star cluster. In this context, FB acts as a delay mechanism, favouring lower stellar densities with a longer relaxation time-scale,

allowing the longer survival of the initial substructure and a more extended final distribution.

3.4 Stellar dynamics

In this section, we focus on the dynamics of individual stars and study the influence of the star cluster formation scenario. Our interest is on escaping stars, due to various dynamical interactions in the densest regions of the star cluster. We then study binary stars, as they are the most likely source of escaping stars during the early phase of the life of the star cluster.

3.4.1 Escaping stars

Escaping stars are particularly interesting when they are massive: they can travel long distances in the Galaxy and eventually explode as supernova (SN) in a location far from their original birthplace, typically in the diffuse ISM. In the kiloparsec-scale simulations of Hennebelle & Iffrig (2014) and Iffrig & Hennebelle (2015), the global SFR in the Galaxy was reproduced if SNe were allowed to explode up to 20 pc from their natal cloud, while ‘homebred’ SN explosions were much weaker in suppressing star formation. Similarly, Gatto et al. (2015) showed that allowing SN to explode at random positions, rather than at density peaks significantly changes the properties of the ISM, resulting in a hot gas filled volume ISM in the first case and a filamentary, hot gas deprived ISM in the second one. Thus, being able to predict the correct number of escaping massive stars to be used as input in galactic-scale simulations is of vital importance.

Escaping stars (or for short ‘escapers’) are usually categorized into ‘walkaway stars’ and ‘runaway stars’.⁴ Runaway stars (RS) are defined as stars with velocities larger than 30 km s^{-1} (Blaauw 1961), produced either by SN explosion in a tight binary system, during which the companion star of the SN gets expelled (Portegies Zwart 2000; Eldridge, Langer & Tout 2011) or through dynamical ejection due to very close, three body encounters with massive stars (Banerjee, Kroupa & Oh 2012; Perets & Šubr 2012; Oh & Kroupa 2016). In this section, we focus only on the latter mechanism, while the former can be thought of as a direct consequence of the multiplicity function which we will discuss in the next section. Walkaway stars (WS, velocities lower than 30 km s^{-1}) are normally defined as ‘slow escapers’, since these are slowly moving stars ejected through normal relaxation processes, such as evaporating stars through distant two-body encounters with other single stars or soft binaries (Spitzer 1987).

In Fig. 11, we plot the modulus of velocity versus position of all stars in the cluster. The size of the symbols is proportional to the mass of the star. Filled symbols indicate single stars, while open circles denote stars which are part of a multiple system (binary, triple or more). The escape velocity is computed as a function of radius (green solid line in Fig. 11), assuming spherical symmetry, which is a good approximation at $t = 2$ Myr (see Fig. 10), by averaging over the individual escape velocities at different positions within the same spherical shell.

⁴ Hypervelocity stars are here considered an extra category, which is not treated in this work. These stars are thought to have a Galactic Centre origin (Brown et al. 2005), probably resulting from close encounters between binary systems and the central supermassive black hole. They reach velocities of $\sim 1000 \text{ km s}^{-1}$, and hence they are actually unbound from the Galaxy. The current fraction of known hypervelocity stars is $\sim 10^{-8}$ per cent of all stars in our Galaxy (Brown et al. 2007).

³ The correlation length is defined as the mean separation between stars in the cluster.

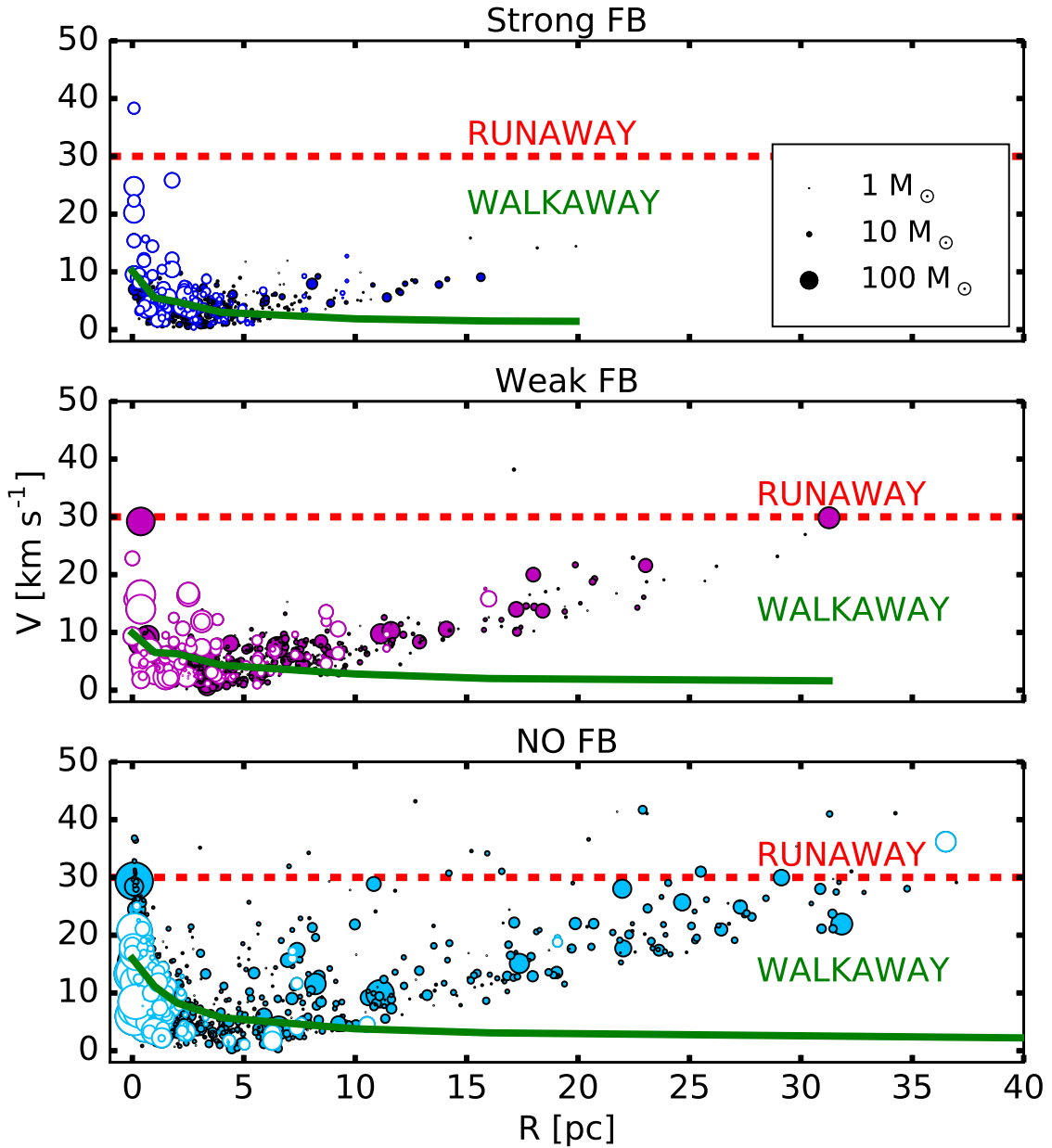


Figure 11. Velocity–position diagram of all stars in the cluster for all three simulations at $t = 2$ Myr. The symbol size is proportional to the stellar mass. Filled circles: single stars. Open circles: stars which are part of multiple systems (binaries, triple systems, etc.). The dashed red horizontal line indicates the conventional velocity above which stars are classified as ‘runaway’. The solid green line indicates the escape velocity.

The no-FB case exhibits the highest number of RS candidates,⁵ namely 31, or about 2 per cent of the total number of stars in the cluster. In the cases with FB, the number of RS is lower, only 1 and 3 in the strong and weak FB, respectively, accounting only for 0.1 and 0.4 per cent of the total number of stars. The RSs in our simulations are generally only massive stars (38, 229, 132, $2 M_{\odot}$)

⁵ It is important to clarify that in Fig. 11 for binaries, triple systems and more, we plot the true velocity, not the velocity of the centre of mass of the multiple system. Thus, some very high velocity binary members are actually still bound. In the computation of the number of RS we did not correct for this; hence, we prefer to talk about RS ‘candidates’, meaning that some are probably not unbound yet, but very likely to be, due to frequent interactions with other particles.

in the FB cases, while in the no FB they cover the whole mass spectrum, going from 0.15 to $417 M_{\odot}$. The fact that RS are close in mass to the most massive stars in the cluster is easily explained considering the mechanism through which these fast stars formed. Indeed, RS are originated as escaping members of perturbed binary systems, which in our case are mostly composed by massive stars. Due to three body interactions, the lighter member of the binary can escape. RS will therefore have very high masses, close in mass but still lighter than the original massive companion.

Regarding WS, the fraction changes slightly depending on the exact definition used. A first possibility is to take all stars with velocity higher than the escape velocity at a given radius and lower than 30 km s^{-1} . This gives us a percentage of WS similar in all simulations, around 30 per cent. If we remove stars in multiple systems

Table 1. Statistics about escapers and multiple systems for all simulations (Strong FB, Weak FB, No FB). In brackets are indicated the percentages, when relevant.

	Strong	Weak	No FB
2-body systems	51	39	40
3-body systems	9	9	5
>3 body systems	6	5	5
Tot multibody system	66	53	50
Stars in multibody system	155 (19 per cent)	126 (15 per cent)	150 (11 per cent)
with $M > 1 M_{\odot}$	128 (31 per cent)	109 (20 per cent)	129 (12 per cent)
with $M > 10 M_{\odot}$	70 (55 per cent)	78 (39 per cent)	94 (24 per cent)
Bound stars	510 (62 per cent)	473 (57 per cent)	900 (64 per cent)
Unbound stars	315 (38 per cent)	355 (43 per cent)	502 (36 per cent)
Runaway	1 (1‰)	3 (4‰)	31 (2 per cent)
of which in multisystem	1	0	2
Walkaway	230 (28 per cent)	297 (36 per cent)	476 (34 per cent)
of which in multisystem	60 (7 per cent)	50 (6 per cent)	39 (3 per cent)

that are still bound (see Footnote 2), then the fraction is reduced to 20 per cent. The final option is to consider WS only in the outskirts of the star cluster, in order to avoid counting stars that are only momentarily unbound. If we call R_{esc} the radius at which the escape velocity becomes comparable to the average stellar velocity at that radius, we can impose the extra requirement to be at a distance greater than $R_{\text{esc}} \simeq 5$ pc from the centre of the star cluster. In this case, we get a very conservative estimate of the fraction around 15 per cent of the total number of members of the cluster.

Table 1 gives an overview of the statistics for escaping stars and multiple systems. We also report the fractions of bound and unbound stars, derived by calculating the kinetic and potential energy for every star, and then verifying whether the sum of the two energies is negative and positive, respectively. In all simulations, the fraction of bound stars is about the same, around 60 per cent.

Comparing the populations of RS and WS in the three simulations, we find that the run without FB produces much more fast escaping stars than the two FB cases. This is consistent with our conclusions in the previous sections, of a very dense star cluster hosting a central clump of tight multiple systems of fast massive stars. Three-body interactions can cause the violent ejection of a member of a binary, of the perturber or of the entire binary system (see Fig. 11). In the FB cases the central densities are lower, and therefore RS stars are rare events.

The number of WS follow the same trend, with the strong FB case having slightly less WS stars than the weak and no-FB cases. Strong FB leads to the less frequent interactions, owing to the lower stellar density, which slows down the evaporation of the stars. We also notice that the different conditions in the three runs have an effect on the typical velocity and mass of WS. In the strong FB case, they do not reach velocities higher than 10 km s^{-1} and are mostly low-mass stars, probably escaping due to several repeated low-energy kicks, typical of evaporation, while in the no-FB case both low- and high-mass stars can reach velocities close to the RS limit of 30 km s^{-1} , as a result of direct ejection.

3.4.2 Multiple systems

We focus now on the analysis of multiple stellar systems. We identify candidate multiple systems by analysing all possible pairs of stars from the cluster. For each pair we calculate the internal energy,

as the total energy of the system in the frame of their centre of mass (Binney & Tremaine 1987):

$$\tilde{E} = \frac{1}{2} \mu v_{12}^2 - \frac{G m_1 m_2}{r_{12}}, \quad (5)$$

where m_1 and m_2 are the masses of the two stars, $\mu = m_1 m_2 / (m_1 + m_2)$ is the reduced mass, v_{12} is the relative velocity, r_{12} the relative distance between the two stars and G is the gravitational constant.

We define the two stars as a binary when $\tilde{E} < 0$. We consider all the binary connections as edges in a graph, whose nodes are all the stars involved in multiple systems. We use graph reduction algorithms to extract which edges share the same nodes, and we group the nodes together, defining triple, quadruple or quintuple systems in this way. For example, two binary systems, (i, j) and (j, k) , which share one node, are considered a triple system.

A slightly different technique was used by Bate (2009) to identify multiple systems. They replaced the binary systems with a virtual star sitting at the centre of mass and with mass equal to the sum of the two masses. They then searched for isolated stars with a negative binding energy with these virtual stars. The same procedure was iterated only up to quadruple systems.

An advantage of our graph-based method is that we can easily identify systems with multiplicity larger than 4. However, in most cases the two algorithms will produce the same catalogue of multiple systems, since, in our case, most multiple systems include a massive star, which dominates the gravitational potential of the system (see Fig. 12).

In Table 1, we report on the statistics of binary, triple and more than three-body systems for all three simulations. We note that the fractions of stars in multiple systems, also known as the multiplicity fraction, correlate with the strength of FB, with overall percentages spanning from 11 per cent (no FB) to 19 per cent (strong FB). If we exclude stars with mass lower than $1 M_{\odot}$, the multiplicity fraction differentiates even more between the three FB regimes and rises to 12, 20 and 31 per cent for no, weak and strong FB, respectively. For stars, with mass greater than $10 M_{\odot}$, the fraction goes up to 24, 39 and 55 per cent. Due to the adopted sink density threshold, fragmentation is not fully resolved for low-mass stars, which might contribute to lower the multiplicity fraction of low-mass stars. A more detailed study focused on the multiplicity of low-mass pre-stellar cores was performed by Lomax et al. (2015).

The observed multiplicity fraction is around 20 per cent, when one considers field stars and low-mass stars, but reaches 60 per cent

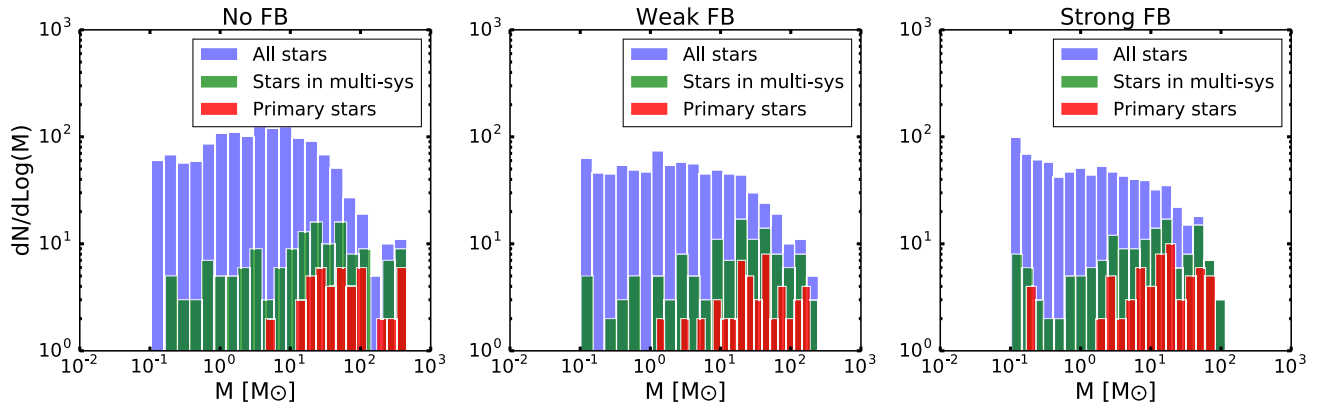


Figure 12. Mass diagrams of stars in multiple systems. The blue histogram reports the total mass function of the cluster. In green we show only stars which are member of multiple systems (binaries, triple, >3) and in red we plot the mass of the primary star, intended as the most massive star in the multibody system. Most multiple systems contain at least one star with $M > 10 M_{\odot}$. In the case with FB, we have also some systems composed only from low-mass stars.

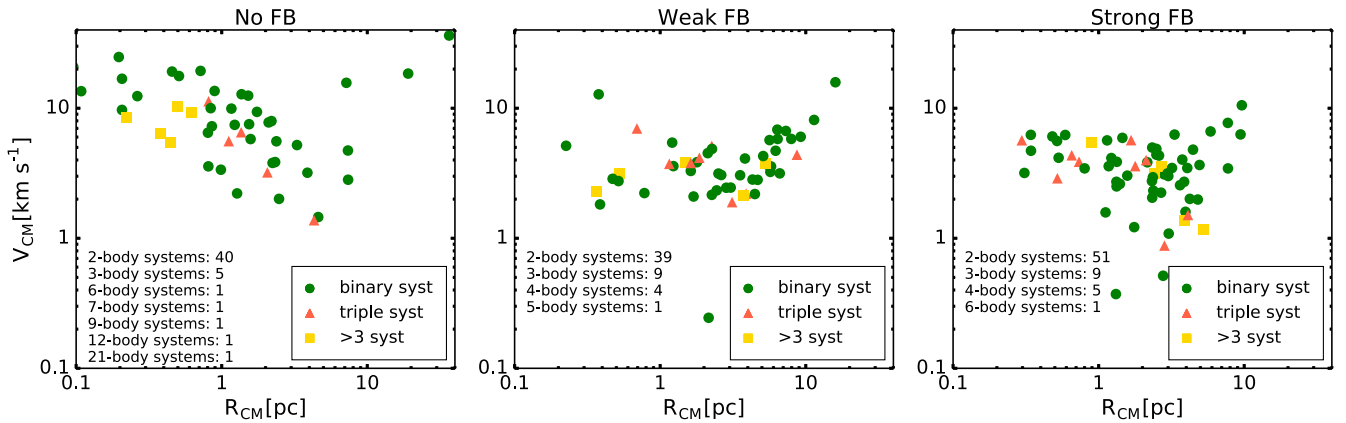


Figure 13. Velocity–position diagram of multiple systems (binary, triple, > 3) in the cluster for all three simulations. We consider velocities (V_{CM}) and positions (R_{CM}) of the centres of masses of the multisystems of stars. In the text, we give details about the statistics of the systems.

for OB and massive stars (Kraus & Hillenbrand 2007; Lafrenière et al. 2008; Goodwin 2010). These values are well reproduced by our strong FB case, while our no-FB run underestimates the number of stars in multiple system, when compared to observations, especially for massive stars. Observations also reveal that the binary fraction is higher in lower density star-forming regions, like in our strong FB case, while denser clusters exhibit multiplicity fractions comparable to the field or low-mass stars, like in our no-FB case (Reipurth et al. 2007; Lafrenière et al. 2008).

In Fig. 13, we plot the distribution of multiple systems in terms of position versus velocity. Here, we consider the positions and the velocities of the centres of masses, explaining why velocities are lower than in Fig. 11. In general, we observe that in the FB simulations binary, triple and more than three-body systems are uniformly distributed throughout the cluster, while the no-FB case shows many systems with very high multiplicity in the very inner part of the cluster, while binaries and triple systems occupy the outskirts. In all cases, we see many ejections of binary systems.

In the same plot, we also indicate the exact count of multiple systems, in particular for groups with more than three bodies. We notice that the maximum multiplicity reaches a much higher value in absence of FB, due to the very high stellar density. With FB, the most crowded multiple systems have 5 or 6 members, while in the no-FB run we have systems with as many as 9, 12 and 21

members. All these high-multiplicity systems are highly unstable and they will be destroyed during the subsequent dynamical evolution of the cluster. As a matter of fact, we do not observe such systems in real star clusters.

In the strong FB case, the lower stellar density will also guarantee the survival of the binary systems, which otherwise, like in the no-FB case, aggregate in bigger associations or are destroyed in three-body interactions. In that context, it is useful to divide binaries into two categories, *soft* binaries and *hard* binaries. Soft binaries are systems for which $|\tilde{E}| < \bar{K}$, while hard binaries have $|\tilde{E}| > \bar{K}$, where \bar{K} is the typical kinetic energy of the stars in the cluster (Binney & Tremaine 1987). We use here the median kinetic energy. According to this definition, for the two FB cases, we have 50 per cent hard and 50 per cent soft binaries, while the no-FB case shows only 30 per cent hard and 70 per cent soft binaries, which support even more our conclusion that binaries will survive longer in the strong FB case.

In Fig. 14, we plot the time evolution of the number of binary, triple and more than three-body systems. In all three models, the number of triple (or more) systems is almost constant. This is not the case for the number of binaries. In the strong FB case, it increases sharply during cloud collapse and after the gas has been dispersed around 1 Myr, it slowly decreases. No additional stars are created and the soft binaries get destroyed through ejection or evaporation.

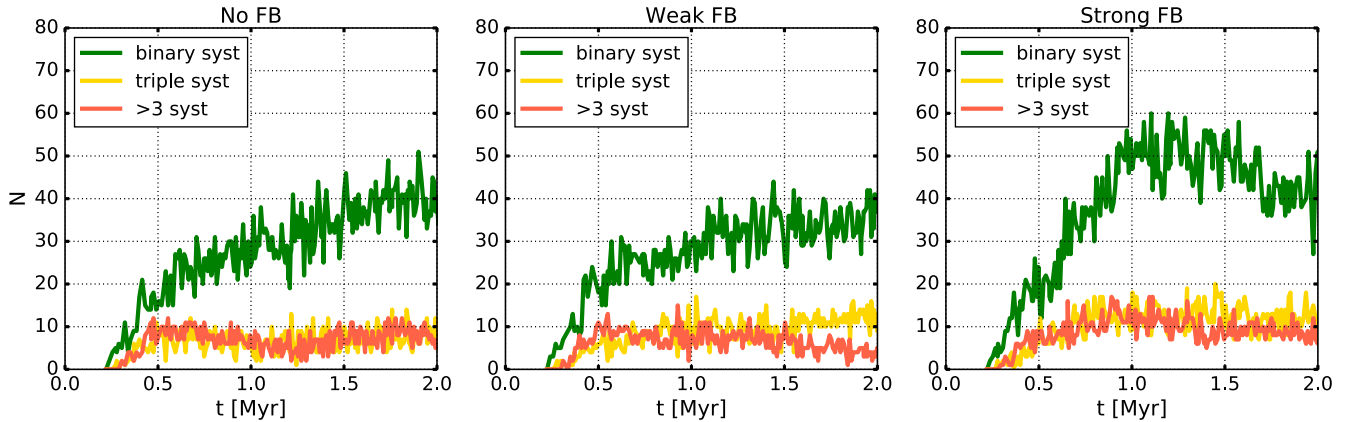


Figure 14. Evolution with time of the number of multiple systems (binary, triple, > 3).

In the no-FB case, the number of binaries keeps increasing since star formation continues until the end of the simulation. The weak FB case shows an intermediate behaviour, with a mild initial increase, followed by an almost constant evolution.

4 SUMMARY AND DISCUSSION

In this work, we have performed radiation hydrodynamics simulations of a collapsing turbulent molecular cloud with the adaptive mesh refinement code *RAMSES*. We have studied in detail the emergence of the star cluster from the parent gas cloud with and without the influence of photoionization FB. Stars are modelled using a sink particle algorithm. Photoionizing radiation is included with two different regimes: weak and strong FB. We also perform a reference simulation without any FB. Our main focus is the emerging properties of the star cluster, both from a structural and a dynamical point of view.

The main effect of photoionization FB is to reduce considerably the stellar density of the star cluster and to limit the accretion on very massive stars. This has a large impact on the dynamical properties of the final star cluster. As a result of the reduced stellar density, the star cluster can settle in virial (or even sub-virial) state, while in the absence of FB, strong and frequent close interactions in a highly collisional environment lead to the disruption of the cluster. This is in contrast with the traditional view that strong FB is responsible for the star cluster early mortality, by rapidly removing gas from the emerging cluster (Hills 1980). The SFE can be reduced down to 20 per cent, without affecting the virial equilibrium of the star cluster.

The stellar mass function is also affected at the high-mass end, with a clear self-regulating role played by FB, limiting the mass of the most massive stars by a factor of 4 compared to the no-FB case. As a result, our mass function with strong FB compares favourably with observations of two starburst clusters (NGC 3603 and Arches) but only after re-normalizing the data and for masses larger than $10 M_{\odot}$.

We also use mass segregation statistics to test our model. In absence of FB, the higher stellar density causes an unrealistically too high degree of mass segregation for a few very massive stars. When including strong FB, we obtain a more extended star cluster with a degree of mass segregation consistent with the one observed in NGC 3603.

We have also computed the number of ejected stars, which anticorrelates with the FB strength: for weaker FB, we get a higher

stellar density and more stars are escaping, both as runaway and walkaway stars. This result has profound implications for galactic evolution, when SNe will start exploding at later time in a large variety of galactic environments.

Our statistics of multiple systems of stars supports the same conclusion: in a denser environment, the fraction of stable binary systems is lower, and most stars tend to either cluster into unstable many-body systems, or are ejected. On the other hand, in the strong FB case, the lower stellar density guarantees the survival of a higher fraction of binaries, in better agreement with observations.

Our results are in line with the findings of Dale et al. (2015, 2012b, 2013b), which showed that photoionization FB effectively lowers the SFE, and, for low-mass clouds like ours, can expel most of the gas within 3 Myr, before the first SN can explode. Parker & Dale (2013), Parker et al. (2015) and Parker & Dale (2015) also observed that photoionization FB reduces the stellar density in the emerging cluster, which allows substructures to survive longer than in a scenario without FB. However, in contrast with Parker et al. (2015) who did not find any mass segregation in the FB case, we do see a weak mass segregation signature, which is well in agreement with observations. Interestingly, although Fujii (2015) found that a local SFE of at least 50 per cent is necessary for the formation of young massive clusters, we could reach a value as low as 20 per cent and still form a bound star cluster.

Our goal in this work is to better understand the transition from a gas cloud to a stellar cluster, or in other words, from gas dynamics to stellar dynamics. In that context, our direct N -body integrator, a second-order leap frog scheme is probably accurate enough for our relatively short time integration, but its accuracy is far below the required standards in stellar dynamics for longer time-scales. This sets the limit on the runtime of our simulations to a couple of Myr. This explains why, in comparison to Parker et al. (2015), who were able to investigate the long term evolution of the star cluster, we are forced to limit our study to the first 2 Myr.

We have also decided in this work to focus exclusively on photoionization radiation. We have therefore neglected magnetic fields and other radiation processes, but also other important physical processes that could be relevant. SNe explosions, for example, are ignored, but, given the cloud mass we have adopted, all the gas is removed from the star cluster after only 2 Myr and they are therefore irrelevant. For larger cloud masses, however, this would not be the case. We have also ignored the possible role of stellar winds, but these have been shown to be negligible compared to photoionization FB (Dale et al. 2015).

We have also ignored the effect of the UV radiation force (or UV radiation pressure) on the gas dynamics. It has been shown that momentum transfer from photoabsorptions is only relevant for ultra compact H II regions, with densities larger than $10^{-15} \text{ g cc}^{-1}$ and sizes smaller than 10^{-3} pc , completely unresolved in our simulations (see e.g. Rosdahl & Teyssier 2015). More relevant would be the inclusion of lower energy photons, in the optical and infrared range. These propagate from accreting stars through dust grains, and are scattered into new infrared photons. Inside the H II regions we can probably ignore these effects as dust is quickly sublimated at 10^4 K , however, infrared and optical radiation can play a role before massive stars form. Skinner & Ostriker (2015) have shown that infrared radiation has very little impact on the gas removal and on the cloud destruction for realistic values of the dust opacity. Infrared radiation is likely to play a more important role on the fragmentation of molecular cores, but at scales we also do not resolve in our simulations.

In summary, we are able to simulate the collapse of a molecular cloud and the emergence of a star cluster, whose properties are tightly connected to the gas dispersal process. Comparing our results to two observed, very young and still active star cluster, NGC 3603 and Arches, we conclude that an initially sub-virial molecular cloud with a SFE lower than 30 per cent can reproduce observations fairly well. Our analysis provides useful insights also for simulations on galactic scales. Star clusters are indeed the building blocks of galaxy formation and evolution. Understanding in details their properties, such as mass segregation, mass and multiplicity functions and escaping stars statistics, just after they emerged from their parent cloud, is of primary importance for their longer term dynamical evolution, but also for the evolution of their host galaxies.

ACKNOWLEDGEMENTS

We thank the anonymous referee for their thoughtful comments and helpful suggestions. This work is supported by the STARFORM Sinergia Project funded by the Swiss National Science Foundation. We would like to thank Sam Geen, Patrick Hennebelle and Michela Mapelli for useful discussions.

REFERENCES

Adamo A., Östlin G., Zackrisson E., 2011, *MNRAS*, 417, 1904
 Allison R. J., Goodwin S. P., Parker R. J., Portegies Zwart S. F., de Grijs R., Kouwenhoven M. B. N., 2009, *MNRAS*, 395, 1449
 Banerjee S., Kroupa P., Oh S., 2012, *ApJ*, 746, 15
 Bastian N., Goodwin S. P., 2006, *MNRAS*, 369, L9
 Bastian N., Ercolano B., Gieles M., Rosolowsky E., Scheepmaker R. A., Gutermauth R., Efremov Y., 2007, *MNRAS*, 379, 1302
 Bate M. R., 2009, *MNRAS*, 392, 590
 Bate M. R., 2014, *MNRAS*, 442, 285
 Baumgardt H., Kroupa P., 2007, *MNRAS*, 380, 1589
 Beccari G. et al., 2010, *ApJ*, 720, 1108
 Bertelli Motta C., Clark P. C., Glover S. C. O., Klessen R. S., Pasquali A., 2016, *MNRAS*, 462, 4171
 Binney J., Tremaine S., 1987, *Galactic Dynamics*. Princeton Univ. Press, Princeton, NJ
 Blaauw A., 1961, *Bull. Astron. Inst. Neth.*, 15, 265
 Bleuler A., Teyssier R., 2014, *MNRAS*, 445, 4015
 Bleuler A., Teyssier R., Carassou S., Martizzi D., 2015, *Comput. Astrophys. Cosmol*, 2, 5
 Bonatto C., Santos J. F. C., Jr, Bica E., 2006, *A&A*, 445, 567
 Brandner W., 2008, in Beuther H., Linz H., Henning T., eds, *ASP Conf. Ser. Vol. 387, Massive Star Formation: Observations Confront Theory*. Astron. Soc. Pac., San Francisco, p. 369

Bressert E. et al., 2010, *MNRAS*, 409, L54
 Brown W. R., Geller M. J., Kenyon S. J., Kurtz M. J., 2005, *ApJ*, 622, L33
 Brown W. R., Geller M. J., Kenyon S. J., Kurtz M. J., Bromley B. C., 2007, *ApJ*, 671, 1708
 Cartwright A., Whitworth A. P., 2004, *MNRAS*, 348, 589
 Chen L., de Grijs R., Zhao J. L., 2007, *AJ*, 134, 1368
 Crowther P. A., Schnurr O., Hirschi R., Yusof N., Parker R. J., Goodwin S. P., Kassim H. A., 2010, *MNRAS*, 408, 731
 Cunningham A. J., Klein R. I., Krumholz M. R., McKee C. F., 2011, *ApJ*, 740, 107
 Da Rio N., Tan J. C., Jaehnig K., 2014, *ApJ*, 795, 55
 Dale J. E., 2015, *New Astron. Rev.*, 68, 1
 Dale J. E., Bonnell I., 2011, *MNRAS*, 414, 321
 Dale J. E., Bonnell I. A., 2012, *MNRAS*, 422, 1352
 Dale J. E., Bonnell I. A., Whitworth A. P., 2007a, *MNRAS*, 375, 1291
 Dale J. E., Ercolano B., Clarke C. J., 2007b, *MNRAS*, 382, 1759
 Dale J. E., Ercolano B., Bonnell I. A., 2012a, *MNRAS*, 424, 377
 Dale J. E., Ercolano B., Bonnell I. A., 2012b, *MNRAS*, 427, 2852
 Dale J. E., Ercolano B., Bonnell I. A., 2013a, *MNRAS*, 430, 234
 Dale J. E., Ercolano B., Bonnell I. A., 2013b, *MNRAS*, 431, 1062
 Dale J. E., Ngoumou J., Ercolano B., Bonnell I. A., 2014, *MNRAS*, 442, 694
 Dale J. E., Ercolano B., Bonnell I. A., 2015, *MNRAS*, 451, 987
 Dalgarno A., McCray R. A., 1972, *ARA&A*, 10, 375
 Drissen L., Moffat A. F. J., Walborn N. R., Shara M. M., 1995, *AJ*, 110, 2235
 Eldridge J. J., Langer N., Tout C. A., 2011, *MNRAS*, 414, 3501
 Elmegreen B. G., 2006, preprint ([astro-ph/0610679](https://arxiv.org/abs/astro-ph/0610679))
 Espinoza P., Selman F. J., Melnick J., 2009, *A&A*, 501, 563
 Federrath C., 2015, *MNRAS*, 450, 4035
 Feigelson E. D. et al., 2013, *ApJS*, 209, 26
 Figer D. F., 2004, in Lamers H. J. G. L. M., Smith L. J., Nota A., eds, *ASP Conf. Ser. Vol. 322, The Formation and Evolution of Massive Young Star Clusters*. Astron. Soc. Pac., San Francisco, p. 49
 Figer D. F. et al., 2002, *ApJ*, 581, 258
 Fujii M. S., 2015, *PASJ*, 67, 59
 Fujii M., Portegies Zwart S., 2015, *IAU General Assembly*, 22, 2254970
 Fujii M. S., Portegies Zwart S., 2016, *ApJ*, 817, 4
 Gatto A. et al., 2015, *MNRAS*, 449, 1057
 Geen S., Hennebelle P., Tremblin P., Rosdahl J., 2015, *MNRAS*, 454, 4484
 Geen S., Hennebelle P., Tremblin P., Rosdahl J., 2016, *MNRAS*, 463, 3129
 Gilmore G. et al., 2012, *The Messenger*, 147, 25
 Goodwin S. P., 2009, *Ap&SS*, 324, 259
 Goodwin S. P., 2010, *Phil. Trans. R. Soc. A*, 368, 851
 Harayama Y., Eisenhauer F., Martins F., 2008, *ApJ*, 675, 1319
 Hennebelle P., Chabrier G., 2008, *ApJ*, 684, 395
 Hennebelle P., Iffrig O., 2014, *A&A*, 570, A81
 Hillenbrand L. A., Hartmann L. W., 1998, *ApJ*, 492, 540
 Hills J. G., 1980, *ApJ*, 235, 986
 Hopkins P. F., 2012, *MNRAS*, 423, 2016
 Howard C. S., Pudritz R. E., Harris W. E., 2016, *MNRAS*, 461, 2953
 Hui L., Gnedin N. Y., 1997, *MNRAS*, 292, 27
 Iffrig O., Hennebelle P., 2015, *A&A*, 576, A95
 Jeffries R. D. et al., 2014, *A&A*, 563, A94
 Klessen R. S., 2011, in Charbonnel C., Montmerle T., eds, *EAS Publ. Ser. Vol. 51, Star Formation in Molecular Clouds*. EDP sciences, Les Ulis, France, p. 133
 Kraus A. L., Hillenbrand L. A., 2007, *ApJ*, 662, 413
 Kruijssen J. M. D., 2012, *MNRAS*, 426, 3008
 Krumholz M. R., 2014, *Phys. Rep.*, 539, 49
 Krumholz M. R., Klein R. I., McKee C. F., 2012, *ApJ*, 754, 71
 Krumholz M. R. et al., 2014, *Protostars and Planets VI*. Arizona Univ. Press, Tucson, p. 243
 Kruskal J. B., 1956, in *Proc. Am. Math. Soc.*, p. 7
 Kudryavtseva N. et al., 2012, *ApJ*, 750, L44
 Kuhn M. A., Feigelson E. D., Getman K. V., Sills A., Bate M. R., Borissova J., 2015, *ApJ*, 812, 131
 Kuznetsova A., Hartmann L., Ballesteros-Paredes J., 2015, *ApJ*, 815, 27

- Lada C. J., Lada E. A., 2003, *ARA&A*, 41, 57
- Lada C. J., Margulis M., Dearborn D., 1984, *ApJ*, 285, 141
- Lafrenière D., Jayawardhana R., Brandeker A., Ahmic M., van Kerkwijk M. H., 2008, *ApJ*, 683, 844
- Lee Y.-N., Hennebelle P., 2016, *A&A*, 591, A31
- Lejeune T., Schaerer D., 2001, *A&A*, 366, 538
- Lomax O., Whitworth A. P., Hubber D. A., Stamatellos D., Walch S., 2015, *MNRAS*, 447, 1550
- Martins F., Hillier D. J., Paumard T., Eisenhauer F., Ott T., Genzel R., 2008, *A&A*, 478, 219
- McLeod A. F. et al., 2016, *MNRAS*, 462, 3537
- Melena N. W., Massey P., Morrell N. I., Zangari A. M., 2008, *AJ*, 135, 878
- Miller G. E., Scalo J. M., 1978, *PASP*, 90, 506
- Offner S. S. R., Klein R. I., McKee C. F., Krumholz M. R., 2009, *ApJ*, 703, 131
- Oh S., Kroupa P., 2016, *A&A*, 590, A107
- Padoan P., Federrath C., Chabrier G., Evans N. J., II, Johnstone D., Jørgensen J. K., McKee C. F., Nordlund Å., 2014, *Protostars and Planets VI*. Arizona Univ. Press, Tucson, p. 77
- Pang X., Grebel E. K., Allison R. J., Goodwin S. P., Altmann M., Harbeck D., Moffat A. F. J., Drissen L., 2013, *ApJ*, 764, 73
- Parker R. J., Dale J. E., 2013, *MNRAS*, 432, 986
- Parker R. J., Dale J. E., 2015, *MNRAS*, 451, 3664
- Parker R. J., Wright N. J., Goodwin S. P., Meyer M. R., 2014, *MNRAS*, 438, 620
- Parker R. J., Dale J. E., Ercolano B., 2015, *MNRAS*, 446, 4278
- Perets H. B., Šubr L., 2012, *ApJ*, 751, 133
- Portegies Zwart S. F., 2000, *ApJ*, 544, 437
- Portegies Zwart S. F., McMillan S. L. W., Hut P., Makino J., 2001, *MNRAS*, 321, 199
- Reipurth B., Guimarães M. M., Connelley M. S., Bally J., 2007, *AJ*, 134, 2272
- Röllig M. et al., 2011, *A&A*, 525, A8
- Rosdahl J., Teyssier R., 2015, *MNRAS*, 449, 4380
- Rosdahl J., Blaizot J., Aubert D., Stranex T., Teyssier R., 2013, *MNRAS*, 436, 2188
- Rosen A., Bregman J. N., 1995, *ApJ*, 440, 634
- Schilbach E., Kharchenko N. V., Piskunov A. E., Röser S., Scholz R.-D., 2006, *A&A*, 456, 523
- Siess L., Dufour E., Forestini M., 2000, *A&A*, 358, 593
- Skinner M. A., Ostriker E. C., 2015, *ApJ*, 809, 187
- Spitzer L., 1987, *Dynamical Evolution of Globular Clusters*. Princeton Univ. Press, Princeton, NJ
- Sternberg A., Hoffmann T. L., Pauldrach A. W. A., 2003, *ApJ*, 599, 1333
- Stolte A., Grebel E. K., Brandner W., Figer D. F., 2002, *A&A*, 394, 459
- Stolte A., Grebel E. K., Brandner W., Figer D. F., 2003, in De Buizer J. M., van der Blik N. S., eds, *ASP Conf. Ser. Vol. 287, Galactic Star Formation Across the Stellar Mass Spectrum*. Astron. Soc. Pac., San Francisco, p. 433
- Stolte A., Brandner W., Brandl B., Zinnecker H., Grebel E. K., 2004, *AJ*, 128, 765
- Stolte A., Brandner W., Grebel E. K., Lenzen R., Lagrange A.-M., 2005, *ApJ*, 628, L113
- Sung H., Bessell M. S., 2004, *AJ*, 127, 1014
- Sutherland R. S., Dopita M. A., 1993, *ApJS*, 88, 253
- Verner D. A., Ferland G. J., Korista K. T., Yakovlev D. G., 1996, *ApJ*, 465, 487
- Walch S. K., Whitworth A. P., Bisbas T., Wünsch R., Hubber D., 2012, *MNRAS*, 427, 625
- Walch S., Whitworth A. P., Bisbas T. G., Wünsch R., Hubber D. A., 2013, *MNRAS*, 435, 917
- Yusef-Zadeh F., Law C., Wardle M., Wang Q. D., Fruscione A., Lang C. C., Cotera A., 2002, *ApJ*, 570, 665

This paper has been typeset from a \LaTeX file prepared by the author.